Tropopause Folds and Synoptic-Scale Baroclinic Wave Life Cycles

ANDREW B. G. BUSH AND W. R. PELTIER

Department of Physics, University of Toronto, Toronto, Ontario, Canada

(Manuscript received 1 September 1992, in final form 3 June 1993)

ABSTRACT

The linear stability of three midlatitude zonal mean states of varying baroclinicity and barotropy is examined using a primitive equation stability analysis under the anelastic approximation. Each of these basic states includes both tropospheric and stratospheric regions with realistic properties compared with those of the earth's atmosphere in midlatitudes. In all three cases, the fastest growing synoptic-scale modes delivered by the linear stability analysis have wavelengths of approximately 4000 km. The nonlinear evolution of these synoptic-scale modes is explored using a three-dimensional anelastic finite-difference model whose zonal scale is chosen to be equal to the wavelength of the fastest growing mode of linear theory. During the nonlinear evolution of the wave, deep tropopause folds are shown to form (generically) and the depth to which the fold penetrates the troposphere is seen to increase with the baroclinicity of the mean state. These folds, descending along the sloping frontal zones within the parent wave, invariably have their maximum depth of tropospheric penetration located at the southernmost edge of the upper-level wave. This paper focuses on three important issues: 1) the impact of the background baroclinicity on these generic tropopause deformations, 2) the stage in the life cycle of the parent wave at which the deformation reaches its greatest vertical extent, and 3) the physical processes that limit this vertical extent.

1. Introduction

The phenomenon of tropopause fold formation and the correlation of such folds with upper-level baroclinic disturbances has been well documented in the observational literature throughout the past several decades (e.g., Reed 1955; Danielson 1968; Danielson and Hipskind 1980). These observational analyses employed a variety of tracers, including radioactive elements (generated by stratospheric atomic bomb testing), ozone, and potential vorticity to ascertain the detailed spatial structure of tropopause folds, and excellent correlations among these various tracers of stratospheric air were thereby revealed. High ozone counts at the earth's surface that are characteristic of stratospheric air, as pointed out by Danielson and Mohnen (1977), may exceed Environmental Protection Agency standards by an order of magnitude on occasions when the tropopause fold is sufficiently deep. The frequent occurrence of such folds within upper-level baroclinic disturbances has made it possible to recognize observationally the preferred location for their development, demonstrating that the deepest folds are most often found along the southern edge of the upper-level long wave, placing the fold just west of the surface cold front (e.g., Staley 1960; Danielson and Mohnen 1977).

Corresponding author address: Dr. W. R. Peltier, Department of Physics, University of Toronto, Toronto, Ontario M5S 1A7, Canada.

Irreversible mass exchange between the stratosphere and the troposphere is of course an important factor in determining the mean chemical composition of each region. For the stratosphere, the ingress of tropospheric air through the agency of tropical cumulonimbus convection allows measurable constituents such as the water vapor mixing ratio to be employed as a tracer of tropospheric air (e.g., Andrews et al. 1987). The egress of stratospheric air in midlatitudes may be traced using such indigenous quantities as ozone and characteristic potential vorticity values. Of this reverse exchange, large-scale eddies (with their associated tropopause folds) near jet stream regions contribute approximately 20 percent (WMO 1985). For an excellent review of stratosphere/troposphere exchange processes in general, the reader is referred to chapter 5 of *Atmospheric Ozone,* vol. 1 (WMO 1985).

Clearly, the approximation that is often employed in the study of nonlinear baroclinic wave life cycles—that the tropopause may be treated as a rigid lid—precludes fold formation. Analyses conducted on the basis of this assumption have nevertheless provided invaluable guidance to understanding the fundamental process of baroclinic wave development. The incorporation of a deformable boundary between the troposphere and the stratosphere into conventional models of baroclinic wave life cycles, which is required to address the issue of fold formation, allows for the added possibility of the above discussed irreversible mass exchange between the stratosphere and the troposphere.

© 1994 American Meteorological Society

The tropopause folding process, whereby a tongue of stratospheric air with a typical vertical/horizontal aspect ratio of approximately 0.06 penetrates the troposphere, has previously been dynamically explored under the assumption of quasigeostrophic theory by Danielsen and Diercks (1967), on the basis of two-dimensional semigeostrophic theory by several authors (e.g., Hoskins and West 1979; Heckley and Hoskins 1982; Moore 1987), and through the use of a two-dimensional primitive equation model (Gidel and Shapiro 1979). Observational reports of tropopause folds have invariably been based upon the presentation of two-dimensional vertical cross sections through them (clearly the cost of multiple observational flights limits the investigative possibilities), and their three-dimensional structures have had to be inferred on the basis of small numbers of such sections. In Fig. 1 we present an example of one such section based upon analyses reported in Staley (1960). The salient features of this typical structure to which we shall subsequently refer are 1) the locus of fold descent lies within the frontal zone, and 2) the slope of the frontal zone (and also of the fold) decreases below 600 mb compared to its slope above 600 mb.

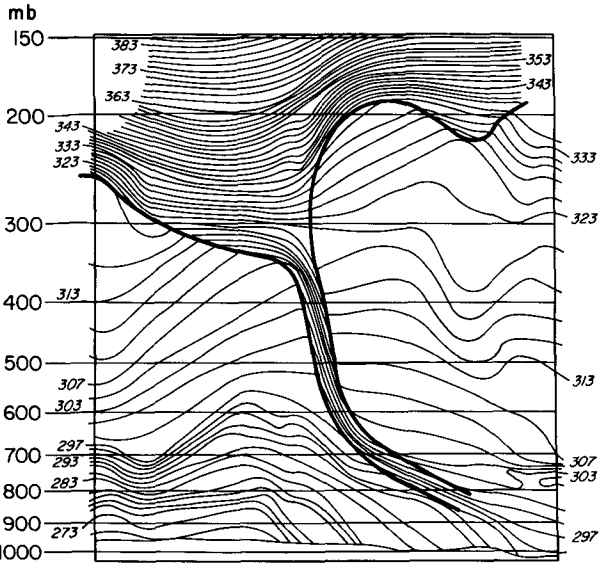

FIG. 1. Vertical cross section through an observed fold from International Falls to Brownsville (a distance of approximately 3000 km), taken from Staley (1960), showing potential temperature and potential vorticity discontinuity.

It is our goal in the present study not only to document the full three-dimensional structure of the tropopause folds induced by the nonlinear baroclinic waves delivered by our numerical simulations, but also to demonstrate the important role played by basic-state baroclinicity in determining the depth to which the fold penetrates into the troposphere. For a specified stratosphere/troposphere buoyancy frequency ratio, this property of the initial zonal flow is the initial determinant of the depth of stratospheric air descent. However, the problem of defining a "realistic" mean state whose stability properties are truly representative of the actual atmosphere is, of course, nontrivial, as any "observed" state has usually been averaged temporally and/or spatially, ensuring that the influence of the eddies is incorporated into the mean. One may nevertheless tentatively suppose that a realistic mean state must lie in some range of baroclinicity/barotropy about an appropriate climatologically averaged state.

The question of the reversibility of the mixing of stratospheric air into the troposphere during the folding process is also of great interest, and Shapiro (1980) has estimated observationally that 50 percent of the mass within a fold is exchanged with tropospheric air during its downward penetration. We will provide an initial numerical exploration of this issue in the analyses to be reported here by employing Ertel's potential vorticity as a tracer. The issue of the extent to which potential vorticity (PV) is conserved by the numerical model in such analyses is clearly important and, as we shall demonstrate, the spatial filters required to inhibit the buildup of noise on the $2\Delta x$ scale do compromise the model's PV invariant somewhat, especially near the time of equilibration of the nonlinear wave. This undermines to some degree the utility of Ertel's PV as a Lagrangian tracer in the model that we employ.

The main results to be described in the present paper are based upon three high-resolution numerical simulations, initialized with mean states of varying baroclinicity. The use of artificial dissipation (mentioned above) allows the simulations to be integrated past the point of occlusion of the synoptic-scale wave, and the results may therefore be usefully compared to the rigid-lid simulations of three-dimensional baroclinic wave development recently reported by Polavarapu and Peltier (1990) based upon the same numerical model. As we shall see, the qualitative evolution of the wave at the lower surface is relatively unaffected by the presence of the deformable tropopause, a result that is consistent with previous analyses based upon semigeostrophic theory (Heckley and Hoskins 1982). Nevertheless, the descent of stratospheric air into the surface cyclone through a deep tropopause fold will be shown to significantly alter the energetics of the classic baroclinic wave life cycle.

The paper is organized as follows. In section 2 we introduce the mean states and describe the linear stability analyses on the basis of the results of which the nonlinear model is initialized. The numerical model itself and the details of the nonlinear simulations that we have performed with it are described in section 3. Our conclusions are presented in section 4 along with a summary of our main results.

2. Initial mean states and linear stability analyses

To initialize the nonlinear model for the purpose of studying the baroclinic instability process, we require

a background state upon which a small amplitude fluctuation may be superimposed. The structure of this fluctuation will be determined through a linear stability analysis of the two-dimensional zonal mean state, defined by specifying a potential temperature field in a meridional cross section and calculating its corresponding thermally balanced zonal velocity field. The coordinate system that we shall adopt is Cartesian with x the zonal (eastward) coordinate, y the meridional (northward) coordinate, and z the vertical coordinate.

The potential temperature field we specify by the following analytic expression [which is a modified version of that employed by Keyser et al. (1989), with the modifications designed to introduce a realistic closure of the jet at tropopause height]:

$$\Theta_t(y, z) = \Theta_0 + \frac{\Theta_0 N_t^2}{g} z - \frac{\Delta\Theta}{2} \tanh\left[\frac{1}{\delta_\theta}\left(\frac{y}{w_j} + y_0 - \mu z\right)\right], \quad z < H(y), \quad (2.1)$$

$$\Theta_s(y, z) = \Theta_0 + \frac{\Theta_0 N_s^2}{g} z - \frac{\Theta_0 H(y)\alpha}{g}(N_s^2 - N_t^2) - \frac{\Delta\Theta\alpha}{2} \times \tanh\left[\frac{1}{\delta_\theta}\left(\frac{y}{w_j} + y_0 - \mu H(y)\right)\right] \times \left(1 + \frac{H(y) - z}{3}\right), \quad z > H(y), \quad (2.2)$$

where

$$H(y) = H_0 - \left(\frac{g\Delta\Theta}{2\Theta_0}\right)\left(\frac{1}{N_s^2 - N_t^2}\right) \times \tanh\left[\frac{1}{\delta_\theta}\left(-\frac{y}{w_j} + y_0\right)\right] \quad (2.3)$$

is the tropopause height, $\alpha(y) = \sin[(24 - z)\pi/[2(24 - H(y))]$ (with z measured in kilometers) is a factor introduced in order to smooth the meridional derivative of the potential temperature by a height of 24 km and close the tropopausal jet (roughly consistent with observation), and the factor w_j controls the width of the jet. It is the parameter w_j that we will vary to provide us with mean states of varying baroclinicity. Note that the matching condition at the tropopause $\theta_t(y, H(y)) = \theta_s(y, H(y))$ is satisfied automatically by the above functional representation. The constants to be employed are as follows: $\theta_0 = 273$ K is the reference potential temperature, $N_t = 10^{-2}$ s^{-1} is the tropospheric buoyancy frequency, $(N_s/N_t)^2 = 6$ is the ratio of the stratospheric to the tropospheric buoyancy frequency squared, $\mu = 70$ is the inverse slope of the tropospheric potential temperature field in the meridional direction, and $\delta\theta = 30$ K is a typical meridional potential temperature variation over the length scale $\delta_\theta = 525$ km. The zonal wind field at the surface is then specified to be zero while above the surface it is calculated through a vertical integration of the relation for thermal wind balance:

$$\frac{\partial U}{\partial z} = -\frac{g}{(\Theta_0 f)}\frac{\partial \Theta}{\partial y}. \quad (2.4)$$

The three mean states used in the analyses to be reported here have (i) $w_j = 2$, (ii) $w_j = 1.5$, (iii) $w_j = 1$ with respective jet core velocities of 43 m s^{-1}, 57 m s^{-1}, and 85 m s^{-1}. They are shown in Fig. 2. The parameter values used in defining the mean state potential temperature field were chosen such that when

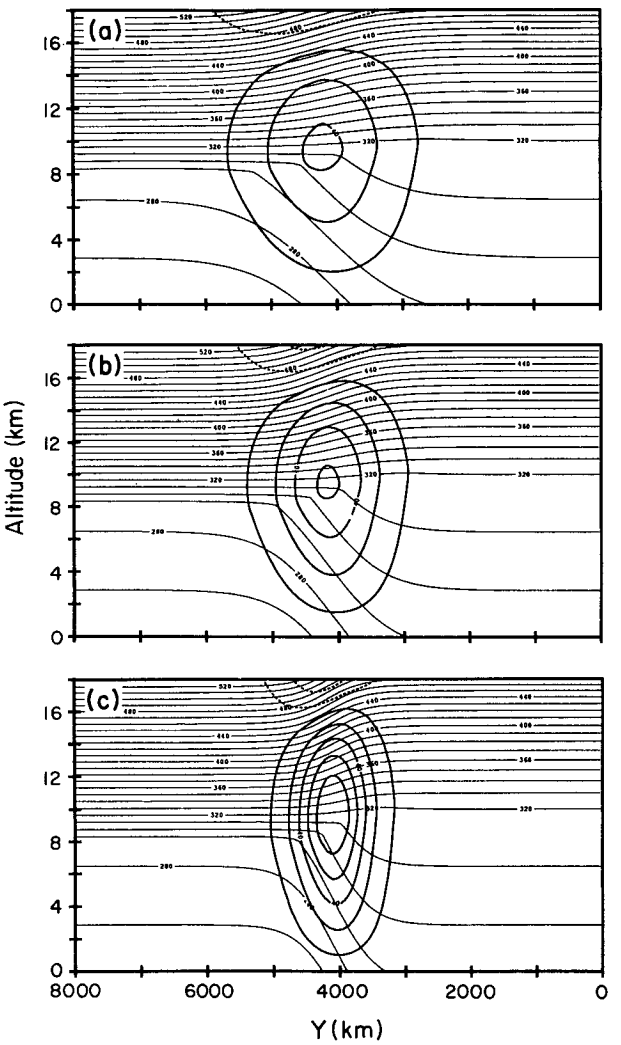

FIG. 2. The three mean states generated by equations (2.1)–(2.4). Thicker contours are zonal velocities with jet maxima of (a) 43 m s^{-1}, (b) 72 m s^{-1}, and (c) 85 m s^{-1} using a contour interval of 15 m s^{-1}. Thinner contours are Θ with a contour interval of 10 K. Values of the parameter w_j in equations (2.1)–(2.3) used to generate the three cases are (a) 2, (b) 1.5, and (c) 1.

$w_j = 2$ (Fig. 2a) the jet resembles the zonally averaged flow over the Northern Hemisphere in winter (Newell et al. 1972). For a winter profile, a tropopause height of 8 km in the north is reasonable (e.g., Holton 1979, p. 121), but the vertical rise of the tropopause as one proceeds south is obviously dependent on the tropospheric and stratospheric buoyancy frequencies. The values of these frequencies employed in (2.3) give a total vertical deflection of approximately 2 km. Since the mean states to be examined have both vertical and horizontal velocity shear, one must expect the possibility of baroclinic, barotropic, and mixed (baroclinic/barotropic) instabilities. The parameters in the analytic expressions determining the background potential temperature field allow us to tune the mean state to any degree of baroclinicity desired, although as the mean state becomes more baroclinic, it also becomes more barotropic because of the increased jet strength (keeping the horizontal scale fixed). One therefore expects to see the eventual dominance of barotropic modes as the zonal velocity in the jet core is strengthened.

The stability of such two-dimensional stratosphere/troposphere mean states has been examined previously (e.g., Simmons and Hoskins 1976, 1977; Gall 1976; Geisler and Garcia 1977), and nonlinear evolution of the fastest growing baroclinic mode of linear theory invariably leads to a vertical deformation of the tropopause (e.g., Heckley and Hoskins 1982). It is clear that the intensity of tropopause folding induced by a parent baroclinic wave will be strongly dependent upon the ratio N_s/N_t. In the limit of sufficiently large values of this ratio the intensity of cyclogenesis at the tropopause will be maximized, but the boundary will be essentially undeformable. In the opposite limit, as the value of this ratio approaches 1, the boundary becomes highly deformable (approaching nonexistent) but upper-level cyclogenesis is suppressed [as in the model of Charney (1948)]. In the analyses to be reported here, we shall not systematically vary the ratio N_s/N_t but rather will fix it to a value (chosen to be $\sqrt{6}$) that delivers a characteristic observed state of the midlatitude atmosphere (Newell et al. 1972). Nevertheless, it should be understood that the value selected for this ratio plays a fundamental role in the fold formation process.

Since the seminal paper on semigeostrophic theory by Hoskins and Bretherton (1972), many frontal and cyclone dynamic processes have been investigated using this approximation since the ageostrophic vertical velocity that it incorporates plays a critical role in realistic baroclinic development. The approximation has also been employed as a basis for the analysis of frontal stability (e.g., Moore and Peltier 1989). Simmons and Hoskins (1976) presented a more complete Boussinesq (hydrostatic) primitive equation stability analysis on the sphere for realistic zonal jets. In Moore and Peltier (1987), a primitive equation methodology for stability analysis in f-plane channels was developed, and this was extended by Polavarapu (1989) to include the influence of both anelasticity and the β effect. The latter methodology will be employed here to explore the linear stability of the mean states discussed above.

In all of the analyses to be presented here we will employ the model embodied in the frictionless, anelastic equations for a dry, adiabatic, inviscid ideal gas on the f plane. The governing equations of this model are, respectively, for conservation of momentum, mass, and internal energy:

$$\frac{D\mathbf{U}}{Dt} + 2\Omega \times \mathbf{U} = -\frac{1}{\bar{\rho}}\nabla p + \left(\frac{\rho}{\bar{\rho}}\right) g\hat{k}, \quad (2.5)$$

$$\nabla\cdot(\bar{\rho}\mathbf{U}) = 0, \quad (2.6)$$

$$\frac{D\Theta}{Dt} = 0, \quad (2.7)$$

in which $\Omega = (0, 0, \frac{1}{2}f)$ is the earth's angular velocity and $\bar{\rho} = \bar{\rho}(z)$ is the background density stratification in the anelastic model. By setting $\partial_t\rho = 0$ in the full continuity equation, the basis of the anelastic approximation that delivers (2.6), sound waves are filtered while retaining the effects of vertical density stratification, effects whose influence on upper-level development is known to be significant (e.g., Hoskins 1972). The results to be described below were all obtained under this approximation; parallel analyses for a Boussinesq fluid show that the anelastic approximation, as expected, enhances upper-level structure. A brief outline of the stability analysis will be provided here, while the interested reader should refer to Moore and Peltier (1987) for detail on the Boussinesq analysis, and to Polavarapu (1989) for the generalized β-plane anelastic model.

Upon linearization of Eqs. (2.5)–(2.7) and expansion of the perturbation fields $\Psi' \in (u', v', w', \theta')$ in conventional normal mode form as

$$\Psi'(x, y, z, t) = \mathrm{Re}(\tilde{\Psi}(y, z)\exp(ibx)\exp(\sigma t)), \quad (2.8)$$

in which b is the zonal wavenumber and σ is the complex parameter that defines the growth rate, $\mathrm{Re}(\sigma)$ and the phase speed $c_{ph} = -\mathrm{Im}(\sigma)/b$, we obtain the linear system that governs the stability problem in the form:

$$(\sigma + iUb + V\partial_y + W\partial_z)\tilde{u} + (\tilde{v}\partial_y + \tilde{w}\partial_z)U - f\tilde{v} + ib\tilde{\phi} = 0 \quad (2.9)$$

$$(\sigma + iUb + V\partial_y + W\partial_z)\tilde{v} + (\tilde{v}\partial_y + \tilde{w}\partial_z)V + f\tilde{u} + \partial_y\tilde{\phi} = 0 \quad (2.10)$$

$$(\sigma + iUb + V\partial_y + W\partial_z)\tilde{w} + (\tilde{v}\partial_y + \tilde{w}\partial_z)W - \frac{g}{\theta_0}\tilde{\theta} + \partial_z\tilde{\phi} = 0 \quad (2.11)$$

$$(\sigma + iUb + V\partial_y + W\partial_z)\tilde{\theta} + (\tilde{v}\partial_y + \tilde{w}\partial_z)\Theta = 0 \quad (2.12)$$

$$\partial_x\tilde{u} + \partial_y\tilde{v} + \left(\partial_z + \frac{d_z\bar{\rho}}{\bar{\rho}}\right)\tilde{w} = 0, \quad (2.13)$$

in which we have introduced the geopotential ϕ.

The mean state, defined for $0 < y < 2L$, is then assumed to replicate over a domain of meridional extent $0 < y < 4L$, allowing the perturbation amplitudes $\tilde{\Psi}$, now defined such that $\tilde{\Psi}(y, z) = \tilde{\Psi}(2L - y, z)$, to be expanded in the following Galerkin form (with the implicit assumption that physical solutions must be localized away from the meridional boundaries):

$$(\tilde{u}, \tilde{v}, \tilde{\theta}, \tilde{\phi}) = \sum_{\lambda=-\infty}^{\infty} \sum_{\nu=0}^{\infty} (U_{\lambda\nu}, V_{\lambda\nu}, \Theta_{\lambda\nu}, \Phi_{\lambda\nu})F_{\lambda\nu} \quad (2.14)$$

$$\tilde{w} = \sum_{\lambda=-\infty}^{\infty} \sum_{\nu=1}^{\infty} W_{\lambda\nu}G_{\lambda\nu}. \quad (2.15)$$

In (2.14) and (2.15), the basis functions F and G are chosen to satisfy the boundary conditions on the perturbation fields and are given by

$$F_{\lambda\nu} = \exp(i\pi\lambda y/2L)\cos(\nu\pi z)$$

$$G_{\lambda\nu} = \exp(i\pi\lambda y/2L)\sin(\nu\pi z).$$

By construction, the boundary conditions on w' of vanishing normal velocity on the upper and lower boundaries are automatically satisfied by the above expansions (in which the vertical coordinate z has been nondimensionalized by the domain height). Orthogonality of the basis functions under the inner product

$$\langle\chi\rangle = \frac{1}{2L}\int_0^{4L}\int_0^1 \chi dxdz \quad (2.16)$$

allows the linearized forms of the field equations to be reduced to the following single matrix eigenvalue problem for the complex amplitude coefficients $U_{\kappa\mu}$, $V_{\kappa\mu}$, and $\Theta_{\kappa\mu}$ after elimination of the vertical velocity and the geopotential:

$$\sigma U_{\kappa\mu} = E_{11}U_{\lambda\nu} + E_{12}V_{\lambda\nu} + E_{13}\Theta_{\lambda\nu} \quad (2.17)$$

$$\sigma V_{\kappa\mu} = E_{21}U_{\lambda\nu} + E_{22}V_{\lambda\nu} + E_{23}\Theta_{\lambda\nu} \quad (2.18)$$

$$\sigma\Theta_{\kappa\mu} = E_{31}U_{\lambda\nu} + E_{32}V_{\lambda\nu} + E_{33}\Theta_{\lambda\nu}. \quad (2.19)$$

The matrix elements E_{ij} for the present problem are provided in the Appendix.

For the results to be shown here, a modified triangular truncation scheme has been employed that allows for 24 waves in the horizontal and 12 in the vertical. Tests of the sensitivity of the results to an increase in the truncation level for all the synoptic-scale waves to be described here were performed, and it was found that as long as at least nine waves were retained in the vertical, the results were insensitive to further increases of the truncation level. Short-wave branches of the growth rate curves (Moore and Peltier 1987) will not be explicitly discussed in the results to be presented below, although they do exist for all the mean states that we have examined. We simply mention in passing that a short, surface-confined, baroclinic mode was found for the state of least baroclinicity that has a very shallow peak at (σ, wavelength) = (0.9 day^{-1}, 1200 km). The long-wave branch visible in all figures is a mixed deep baroclinic/barotropic mode, with the peak of its growth rate at roughly (σ, wavelength) = (1 day^{-1}, 7600 km), similar to that found in Gall (1976) and by most other authors who have examined the problem of baroclinic instability for midlatitude zonal jets.

The growth rate and phase speed curves for the three mean states are presented in Fig. 3, where the zonal wavenumber has been nondimensionalized using a characteristic scale of 2400 km. A synoptic-scale peak in the growth rate spectrum obtains for all three mean states, with the growth rate increasing with the baroclinicity of the meridional temperature field, as expected. The f-plane results shown in Fig. 3a are very similar to those obtained in a quasigeostrophic β-plane model by Simmons and Hoskins (1976). In that study, the maximum in the growth rate spectrum was shown to obtain approximately at (σ, wavelength) = (0.55 day^{-1}, 4100 km). Note the weak variation of phase speed with wavenumber for these modes, a result that is also consistent with the previous findings of Simmons and Hoskins (1976).

Structure functions, defined as the norms of the complex perturbation amplitudes $|\tilde{\Psi}(y, z)|$, for the fastest growing modes of Fig. 3 are shown in Fig. 4. The resemblance of Fig. 4a to the structure function of the symmetric Eady wave is readily apparent, although meridional velocity and potential temperature fluctuations are stronger at the surface (Eady 1949). This mode is also very similar in structure to the wavenumber 6 mode of Simmons and Hoskins (1977), for which there are marked velocity and temperature perturbations at the tropopause, but for which the maximum temperature perturbation is also at the surface. The mode of Fig. 4b for the mean state with intermediate baroclinicity appears to have the same basic structure, with a meridional intensification in response to the increased background baroclinicity. The quadrupole structure in the zonal velocity field apparent in Fig. 4a has become more strongly dipolar in response to this increasing meridional confinement.

The mode of Fig. 4c for the mean state of maximum baroclinicity is, in contrast, strongly focused in the upper region of the jet in the lower stratosphere. The second fastest growing mode for this third mean state is a subharmonic of the first mode, while the third fastest growing mode corresponds to a further meridional tightening of the baroclinic mode of Figs. 4a,b (Fig. 4d).

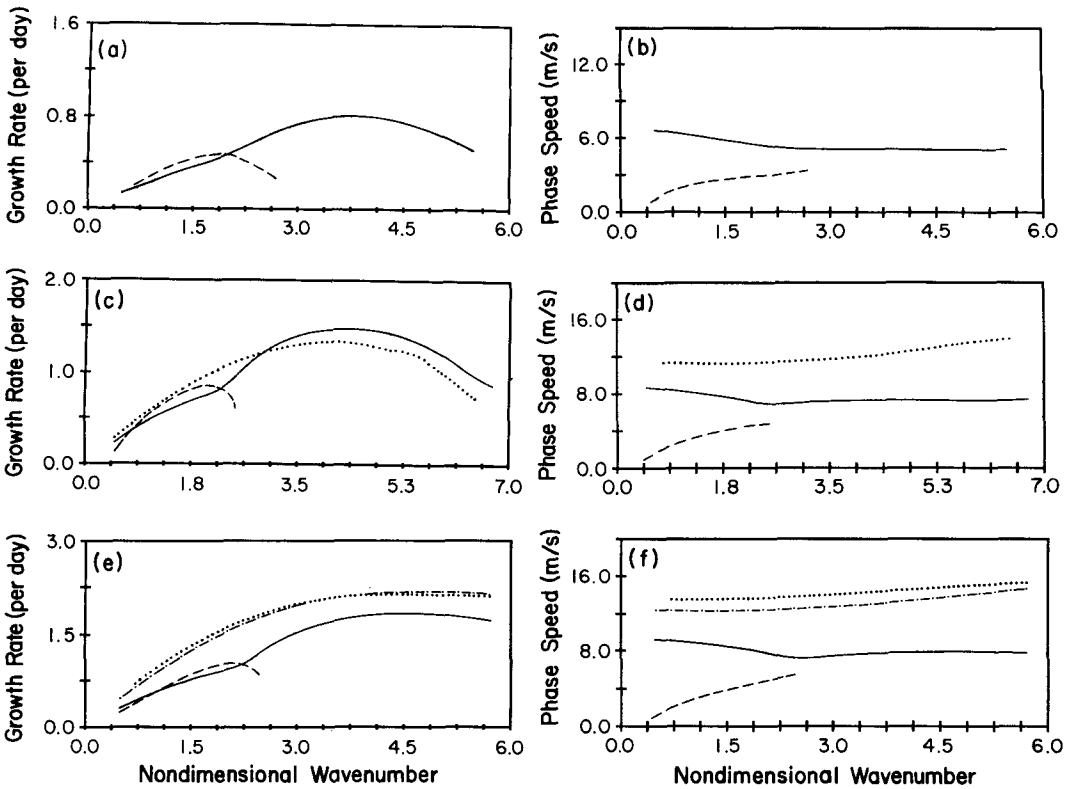

FIG. 3. The growth rate ($\mathrm{Re}(\sigma)$) and phase speed ($c_{ph} = \mathrm{Im}(\sigma)/b$) curves for the relevant modes of the respective mean states of Fig. 2. The wavenumber has been nondimensionalized by 2400 km. Solid lines are baroclinic modes. Note the eventual dominance of the synoptic-scale barotropic mode (dotted line) and the persistence of the mixed baroclinic/barotropic long-wave mode (dashed line).

To illustrate the relative baroclinicity/barotropy of these modes, we show, for simplicity, the quasigeostrophic form of the Eliassen–Palm flux in the Boussinesq limit (i.e., neglecting vertical eddy transfers of heat and momentum). This flux has the form (e.g., Edmon et al. 1980)

$$\mathbf{F} = \left(0, -\rho_0 \overline{u'v'}, \rho_0 f \frac{\overline{v'\theta'}}{\partial_z \bar{\Theta}}\right), \qquad (2.20)$$

where ρ_0 is taken to equal 1 kg m^{-3}. A vertical orientation of the flux vectors indicates a baroclinic mode (i.e., a large eddy heat flux), whereas a horizontally oriented vector indicates a barotropic mode (i.e., a large horizontal momentum flux). Along with its divergence $\nabla \cdot \mathbf{F}$, this flux is shown in Fig. 5 for the fastest growing modes of the respective three mean states presented in Fig. 2. The relative baroclinicity/barotropy of these modes is quantified by the eddy conversion terms, listed in Table 1.

These modal structures, having been suitably normalized so that the maximum temperature perturbation is 0.5 K, are employed in the next stage of analysis as initial perturbations to the respective mean states in order to study their nonlinear development. The length of the domain in the zonal direction is chosen to be equal to the wavelength of the fastest growing mode of linear theory so that we are explicitly favoring modes of that wavelength. However, as will be demonstrated in section 3, this does not automatically imply that the fastest growing mode of linear theory will be the one that is realized in the nonlinear integration.

3. Baroclinic wave life cycles with troposphere–stratosphere exchange

With initial conditions determined as discussed in the previous section, we are in a position to address the issue of the physical processes that occur as the initial baroclinic/barotropic instability matures. Following a cursory discussion of the numerical model to be employed, we will focus upon the nature of the nonlinear life cycles themselves.

a. The numerical model

In order to study the temporal evolution of the perturbed mean states, we shall employ the three-dimensional, anelastic, nonhydrostatic, finite-difference primitive equation model documented in Clark

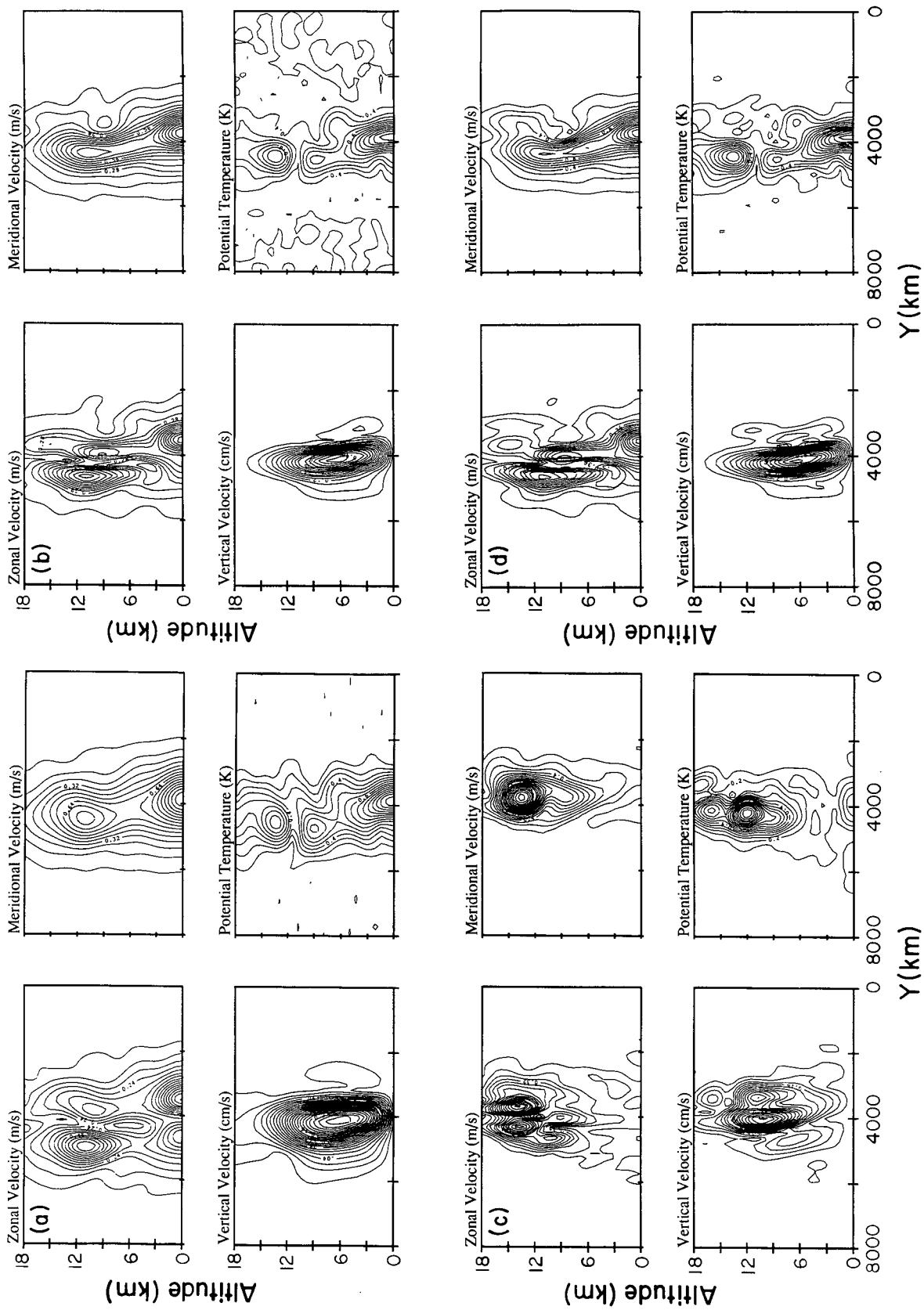

FIG. 4. Structure functions, defined as the norm of the complex perturbation amplitudes, for the three fastest growing synoptic-scale modes of, respectively, Figs. 3a, 3b, and 3c. Included also in Fig. 4d is the baroclinic mode of Fig. 3c. The wavelengths of these modes are (a) 4620 km, (b) 3590 km, and (c) and (d) 3208 km. Note the similarity in the deep structure of the modes of Figs. 4a,b,d and the upper-level confinement of the mode in Fig. 4c.

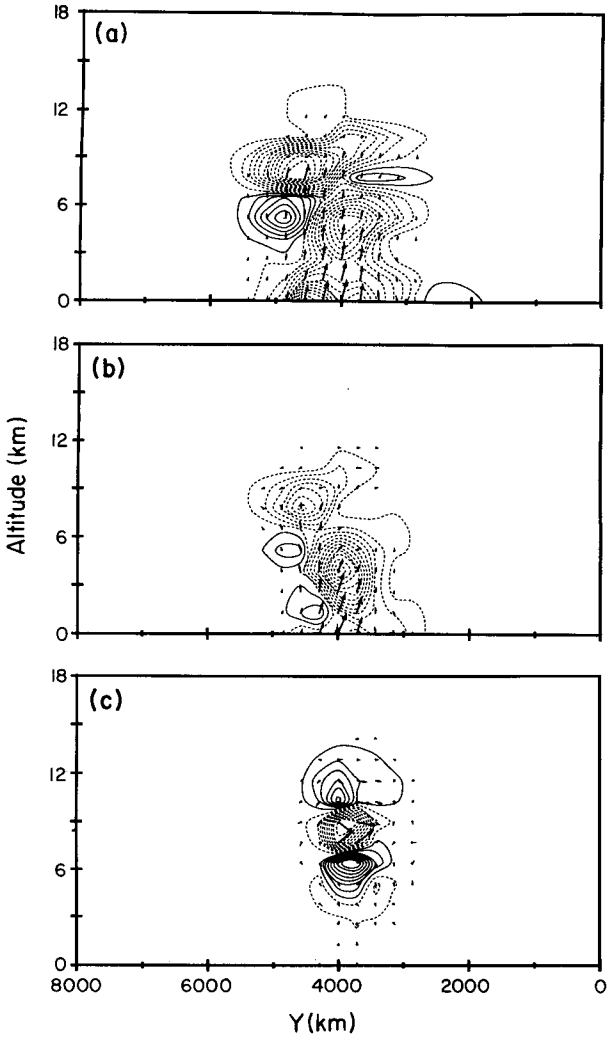

FIG. 5. The quasigeostrophic Eliassen–Palm flux and divergence for the Boussinesq version of the first three respective modes of Fig. 4. Note the deep baroclinic structure of the mode in Fig. 5a, the shallower, more barotropic structure of the mode in Fig. 5b, and finally the dominantly barotropic structure of the mode in Fig. 5c.

TABLE 1. The integrated Reynolds stress (RS = HRS + VRS), horizontal heat flux (HHF), and vertical heat flux (VHF) for the modes of Fig. 4. The values have been scaled so that HHF = 1.

	Mode		
	1	2	3
RS	0.5	2	31.6
HHF	1	1	1
VHF	54.4	50.9	−5

(1977). The model was originally developed as a cloud-scale model, but has, in the course of its evolution, been adapted to study synoptic-scale disturbances (e.g., Polavarapu and Peltier 1990). A schematic of the model domain is presented in Fig. 6. We adopt a channel geometry with rigid walls at $z = 0$, 18 km and at $y = 0$, 8000 km, with periodic boundary conditions in the x (zonal) direction. A ∇^6 spatial filter (hyperviscosity) with a coefficient chosen so that the amplitude of $2\Delta x$ waves is damped by a factor of 10 in ten time steps is implemented in the horizontal plane to allow integration beyond the time at which tight, grid-scale gradients form in the fields associated with, for example, surface frontogenesis. The effects on energy conservation associated with the application of this filter are slight, in that energy is conserved to within a few percent for all simulations at all times. An important point, however, concerns the effect of the filter on potential vorticity conservation [in what follows we will refer to Ertel's (1942) potential vorticity $Q = \boldsymbol{\zeta}\cdot\nabla\theta/\rho$ as PV], since it is this field that is most naturally employed to indicate the location of stratospheric air. As will be discussed in the next section, the model conserves PV to within $\approx$ 0.03 percent of the domain-averaged value up to the time of wave equilibration and occlusion, beyond which the filters, acting on the gradients within the domain, decrease the domain-averaged PV to a value roughly 1 percent lower than the initial value. The range of heights at which PV nonconservation arises was determined by a gridpoint by gridpoint vertical integration. After the fronts become sufficiently tight, positive PV generation onsets at the lower boundary beneath a more significant region of upper-tropospheric PV destruction. This is in contrast to previous tropospheric rigid-lid calculations (Polavarapu and Peltier 1990), in which PV was found to be generated in the frontal zones at both boundaries, and for which there was then a net increase in domain-averaged PV of roughly 40 percent. Note that our averaged PV deviation is extremely small (relative to these previous analyses) only because large stratospheric PV values are included in the averaging.

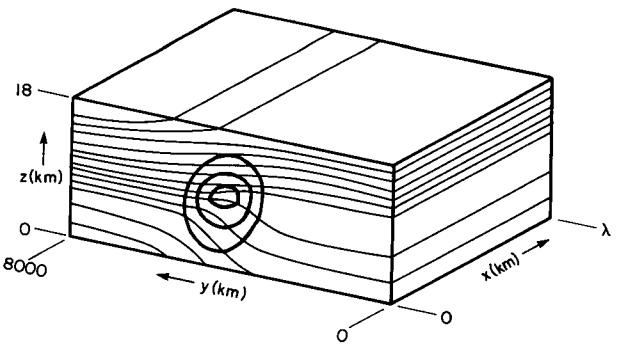

FIG. 6. The channel geometry adopted to study the nonlinear evolution of the perturbed mean states. Free-slip rigid walls are located at $y = 0$, 8000 km and at $z = 0$, 18 km. The zonal domain length is chosen to be equal to the wavelength of the fastest growing mode of linear theory.

In all of the simulations to be reported here, the meridional width of the domain is chosen to be 8000 km in order to ensure localization of the disturbance away from the meridional walls throughout its evolution, and a height of 18 km is chosen in order to position the tropopause roughly at midheight of the domain. It was found that no absorber adjacent to the upper lid was necessary because of the rapid vertical decay of the disturbances above the tropopause.

The numerical details concerning the model grids adopted for the three main simulations we shall discuss are provided in Table 2. For purposes of initialization, it is necessary that the mean state velocity and potential temperature fields be balanced to machine precision (all simulations were run on a Cray XMP-28 at the Ontario Centre for Large Scale Computation in Toronto) to prevent any initial internal wave generation. The time integration of this first-order balanced mean state plus the small amplitude normal-mode perturbation is not expected to deliver perfectly balanced fields in the subsequent evolution, since higher-order terms that are neglected in (2.4) become pertinent. Indeed the solution, as a result of these higher-order terms, exhibits an inertial oscillation that eventually decays over a period of roughly 2–3 days (see also Polavarapu and Peltier 1990), an oscillation that would perhaps be eliminated by a suitable normal-mode initialization scheme (e.g., Leith 1980).

The ability of this nonhydrostatic model to support a realistic spectrum of internal gravity waves is currently being exploited through the diagnosis of balanced versus unbalanced motion in these simulations, the goal being to understand the manner in which a field of internal waves may be spontaneously generated in the course of the life cycle of the predominantly vortical baroclinic wave.

b. Results of the numerical simulations

Given the mean states and their respective fastest growing modes described in section 2, we initialize by superimposing these two ingredients and allowing the model to evolve the fields forward in time. Since there are initial imbalances, however, resulting from the normal-mode perturbation, it is not entirely obvious that the fastest growing mode of linear theory will necessarily remain dominant in the early stages of evolution. In fact, we will see in the third simulation that the inertial oscillations induced by the startup procedure do significantly hamper the growth of the fastest growing mode of linear theory.

1) THE FIRST SIMULATION: CLIMATOLOGICAL BAROCLINICITY

For this initial analysis, the mean state of Fig. 2a and the normal-mode perturbation whose structure is shown in Fig. 4a are combined to initialize the model.

TABLE 2. Domain and grid sizes for the three nonlinear runs.

	Run		
	One	Two	Three
Domain size (x, y, z) km	(4620, 8000, 18)	(3590, 8000, 18)	(3208, 8000, 18)
Grid numbers (x, y, z) km	(68, 126, 28)	(68, 126, 28)	(68, 126, 28)
Grid sizes (x, y, z) km	(65.2, 63.5, 0.6)	(52.8, 63.5, 0.6)	(47.2, 63.5, 0.6)

We will outline here the definitions of the energy and conversion terms that we shall employ for the purpose of diagnostic analysis of the three simulations. By exploiting the zonally periodic boundary conditions, the zonal kinetic energy (ZKE) may be defined as the zonally averaged kinetic energy:

$$\mathrm{ZKE} = \frac{1}{2}\rho\tilde{u}^2, \tag{3.1}$$

where a tilde now denotes a zonal average. The eddy kinetic energy (EKE) may then be defined as the departure of the total kinetic energy from this zonal average:

$$\mathrm{EKE} = \frac{1}{2}[\rho u'^2 + \rho v'^2 + \rho w'^2]. \tag{3.2}$$

The energy budget equations are then as follows:

$$\partial_t[\overline{\mathrm{ZKE}}^{xyz}] = \overline{[\mathrm{HRS} + \mathrm{VRS}]}^{xyz} \tag{3.3}$$

$$\partial_t[\overline{\mathrm{EKE}}^{xyz}] = -\overline{[\mathrm{HRS} + \mathrm{VRS} + \mathrm{VHF}]}^{xyz} \tag{3.4}$$

$$\partial_t[\overline{\mathrm{PE}}^{xyz}] = \overline{[\mathrm{VHF}]}^{xyz}, \tag{3.5}$$

where

$$\bar{\Psi}^{xyz} = \frac{1}{HL_xL_y}\int_0^H\int_0^{L_y}\int_0^{L_x}\Psi dxdydz;$$

$\mathrm{PE} = -\rho g z\theta^*$ is the total potential energy (θ^* is the potential temperature deviation from a constant value), and the terms HRS (horizontal Reynolds stress), VRS (vertical Reynolds stress), and VHF (vertical heat flux) have the following forms:

$$\mathrm{HRS} = -[\rho v u' \partial_y \tilde{u}] \tag{3.6}$$

$$\mathrm{VRS} = -[\rho w u' \partial_z \tilde{u}] \tag{3.7}$$

$$\mathrm{VHF} = -[\rho g w \theta^*]. \tag{3.8}$$

The evolution of the total kinetic energy (KE = ZKE + EKE) and total potential energy (PE) during this simulation is shown in Fig. 7a. Energy is very nearly conserved during the 16-day run, even though the gradients are being smoothed by the diffusion operator beyond approximately day 6.5. The zonal kinetic energy and the eddy kinetic energy for the flow are shown

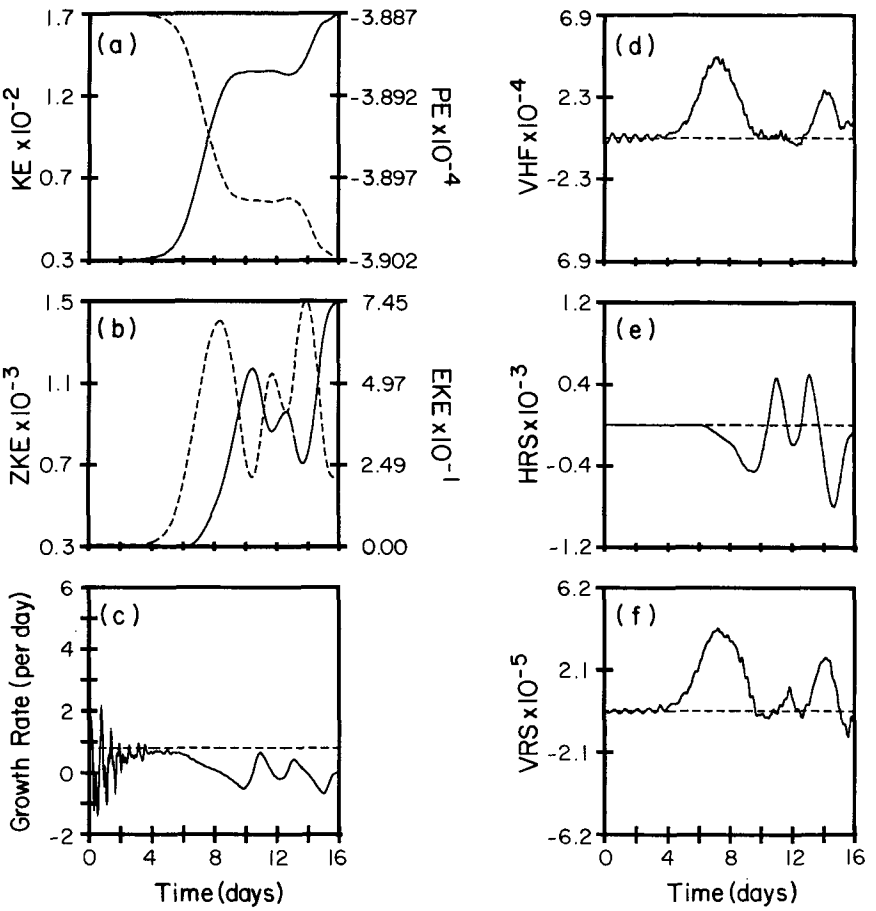

FIG. 7. Time series of the energetics and conversion terms of the nonlinear simulation initialized with climatological baroclinicity. Terms were calculated every 1/2 hour of model time. (a) Total kinetic energy $\times 10^{-2}$ (solid) and total potential energy $\times 10^{-4}$ (dashed), (b) zonal kinetic energy $\times 10^{-2}$ (solid) and eddy kinetic energy $\times 10^{-1}$, and (c) growth rate (see text). Dashed line in (c) marks the result of linear theory. (d) Vertical heat flux $\times 10^{-4}$, (e) horizontal Reynolds stress $\times 10^{3}$, and (f) vertical Reynolds stress $\times 10^{5}$. Units for (a), (b) are J m^{-3} and for (d), (e), and (f) are W m^{-3}.

in Fig. 7b. The linear regime of the initial baroclinic wave coincides with the time during which there is an exponential growth of the EKE. This period lasts until roughly day 6, delineating the regime of validity of linear theory. Figure 7c, in which the growth rate

$$\sigma = \frac{1}{2}\frac{d(\ln \mathrm{EKE})}{dt} \tag{3.9}$$

is plotted against model time, concurs, showing that the growth rate predicted by linear theory (marked by the dashed line) is very close to that exhibited by the growing wave in its initial linear phase. The initial imbalance of the fields is also evident, and the inertial oscillation is seen to persist until roughly day 4.

The baroclinic nature of the wave is clearly displayed in the evolution of the vertical heat flux, the horizontal Reynolds stress, and the vertical Reynolds stress shown, respectively, in Figs. 7d–f. Two distinct episodes of baroclinic growth and barotropic decay, the second episode to be described shortly, are evident at days 4 and 12. Both the energy and conversion terms are calculated every half-hour of model time. The first peak in the EKE, following the period of exponential growth, defines the time of equilibration of the baroclinic wave, and (phenomenologically) the onset of the occlusion process. The second peak in EKE occurs at day 11.5 and coincides with a reformation of the surface and upper-level lows, after they have been zonally elongated by the initial period of barotropic decay. This reformation is clearly a consequence of our having employed zonally periodic boundary conditions in the simulation, and it would not be expected to obtain in a channel model with inflow/outflow boundary conditions (analyses of this kind will be reported in a future

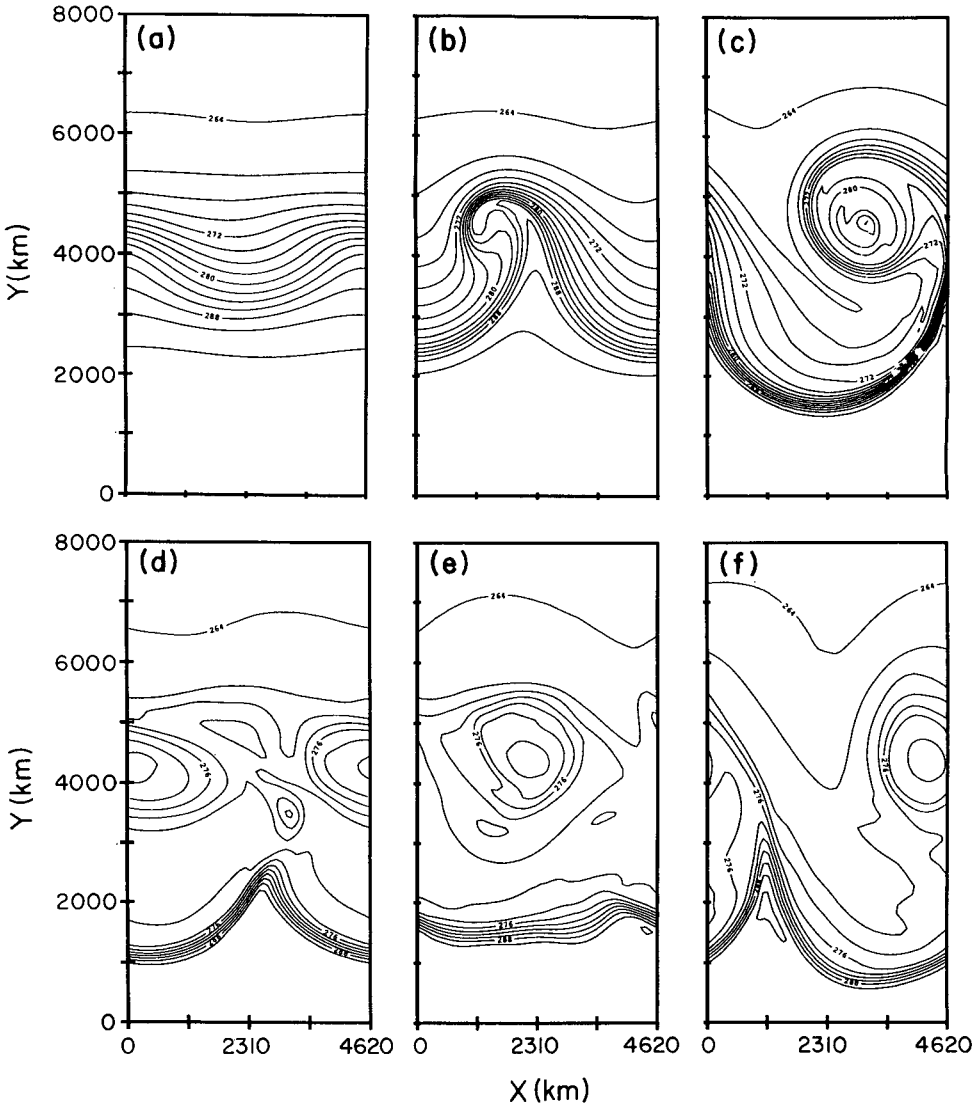

FIG. 8. The evolution of surface potential temperature for the simulation initialized with climatological baroclinicity. The domain is 8000 × 4620 km. The maximum temperature in the core of the low is 285 K and the contour interval is 2 K. (a) Day 4, (b) day 6, (c) day 8, (d) day 10, (e) day 12, and (f) day 14. Note the redevelopment of the surface low at day 12 and the appearance of a new frontal structure at day 14.

publication). The third peak in EKE at day 14 is the result of a surface frontal disturbance. This subsynoptic-scale (300–400 km) baroclinic disturbance appears not to occlude in consequence of the restrengthening of the surface low, and there is a tenuous reconnection of this low to the warm air (see Fig. 8f below). This may be evidence of the stabilizing influence of the external strain field induced by the surface low on the instability of the frontal PV strip (Dritschel et al. 1990).

With the introduction of β-plane effects, the surface low will migrate northward, diminishing its stabilizing influence on the frontal zone and allowing for the possibility of a secondary mesoscale baroclinic development in the surface front. Such a subsynoptic-scale disturbance, whose life cycle mimics that of the parent cyclone, has previously been demonstrated to occur after the time of occlusion in the β-plane simulations of Polavarapu and Peltier (1992).

Because of the periodic boundary conditions that we impose the cyclic nature of the eddy kinetic energy time series would probably continue since, on the f plane, the lows will not migrate meridionally and will continue to zonally elongate, reform, and interact with the frontal zone. It is found, however, that by day 16 the horizontal velocity shear at the surface is so intense that the low is sheared into three distinct fragments, and the

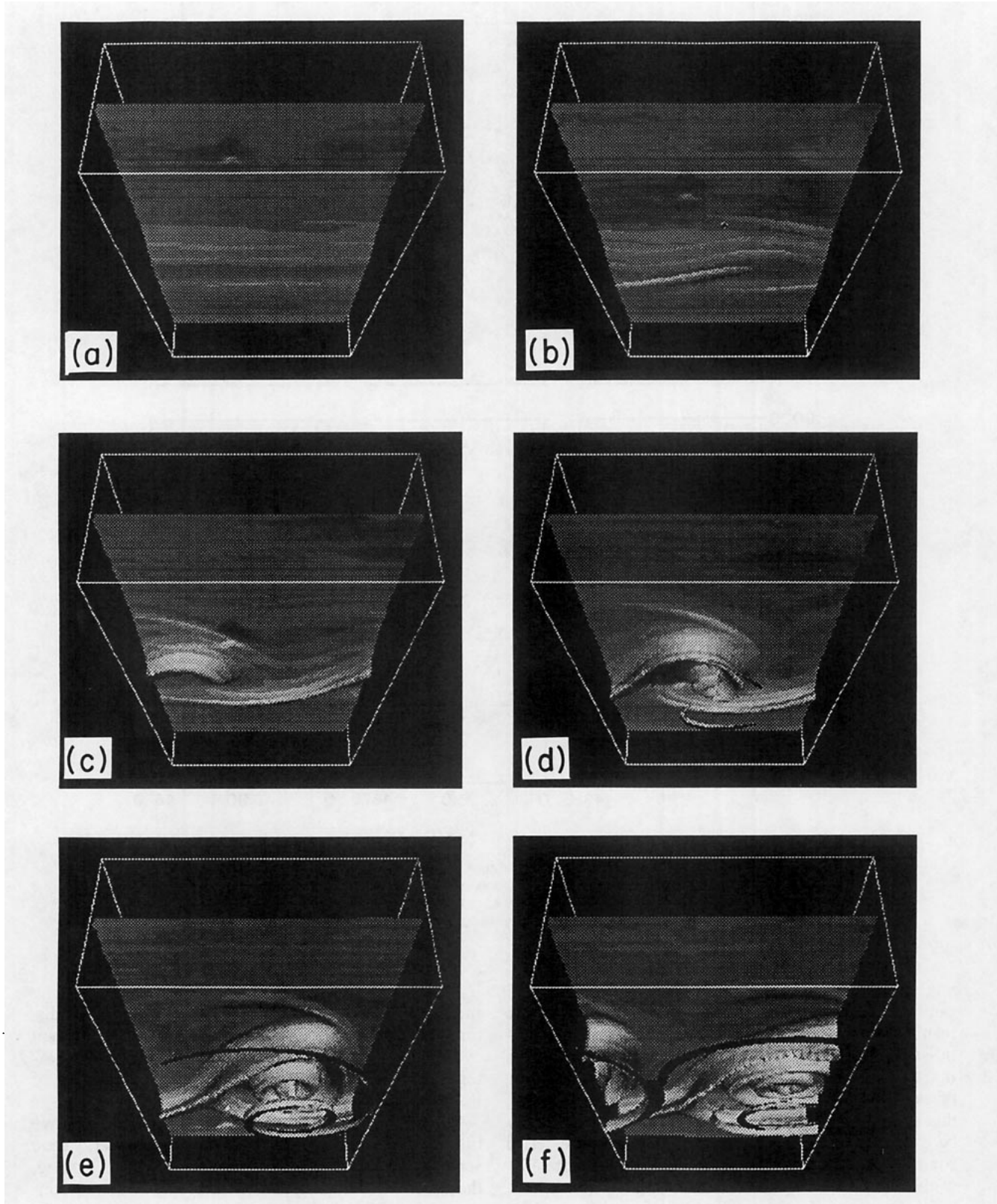

FIG. 9. The evolution of the tropopause (here defined to be the 1×10^{-6} km^2 kg^{-1} s^{-1} surface) for the simulation initialized with climatological baroclinicity. The perspective is such that one is looking upward and northward at a domain that is 8000 × 4620 × 18 km. (a) Day 1, (b) day 4, (c) day 6, (d) day 7, (e) day 8, and (f) day 9. Note the vortical structure of the fold and the boundary-generated PV first visible at day 7 in (d).

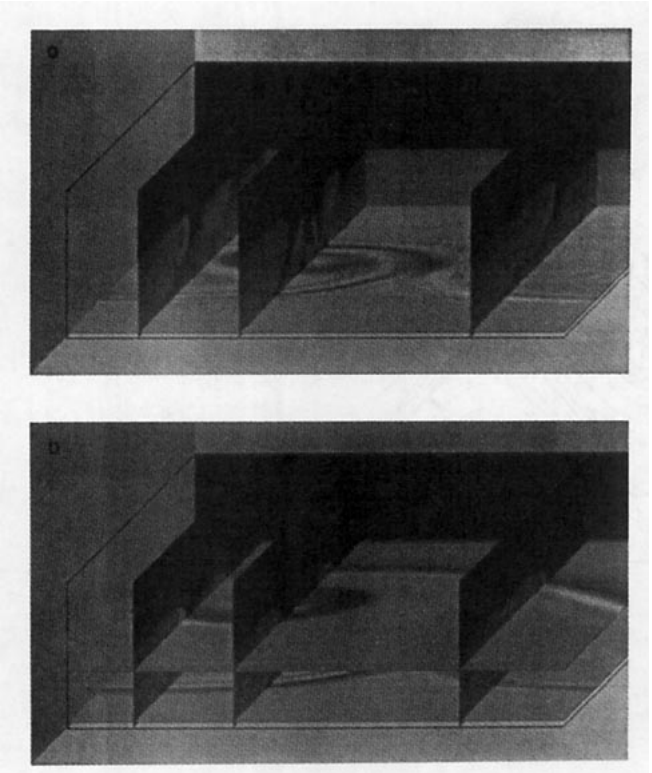

FIG. 10. Cross-sectional plots of Ertel PV at day 6.5 of the first simulation. High values are darker. The perspective is such that one is looking northwest and downward. Note in (a) the high values generated in the surface frontal zones and in (b) the correspondence of the fold with the upper-level wave.

zonal velocity field develops a deep banded structure of alternating westerly/easterly/westerly flow.

The evolution of the surface potential temperature field during this simulation is presented in Fig. 8, and this very much resembles previous high-resolution primitive equation rigid-lid *f*-plane simulations of baroclinic life cycles (Polavarapu and Peltier 1990), with the exception of the secondary baroclinic development in the surface frontal zone. Note in Fig. 8e the flattening of the cusp (i.e., that part of the frontal zone from which the surface low has recently detached), and the instability arising from the same region (cf. Fig. 8f). This disturbance, initially propagating westward, enters the strong circulation around the low and is swept upward and eastward, with a further transfer of warm air to the low. The emphasis we wish to place, however, is on the upper-level development, in which region the deformable tropopause becomes an active contributor to the dynamics.

Figure 9 displays the temporal evolution of the 1 PV unit (PVU = 1×10^{-6} km^2 kg^{-1} s^{-1}) surface, the value being chosen as representative of the tropopause (we will henceforth consider the tropopause to be represented by the 1 PVU surface). The vortical nature of the baroclinic wave and the associated tropopause fold are both clearly evident. Also seen, commencing in Fig. 9d, is the appearance of potential vorticity that has been generated at the lower boundary in the frontal zones by the action of the ∇^6 diffusion operator [see Nakamura and Held (1989) for a discussion of this mechanism in the context of a two-dimensional model]. The deepest vertical extent of the fold occurs in Fig. 9e, in which by 8 days of model time the fold has descended to within a distance of approximately 4 km of the earth's surface. The deepest part of the folds found in all simulations to be reported here invariably occurs, as in observations (e.g., Staley 1960), at the southernmost edge of the upper-level wave, which positions it just northwest of the surface cold front (if we may identify the fronts developed by our simulations in the conventional way). This result is consistent with the dynamics of the baroclinic wave, for which the most intense horizontal deformation, and hence the strongest vertical velocities (which for this low baroclinicity simulation had a maximum negative value of 10 cm s^{-1}), occurs in the frontal regions that slope upward and westward from the surface during the wave's growth. The classic tilt of observed folds (e.g., Danielsen and Mohnen 1977) is a result of this sloping frontal region and the adiabatic motion within it. In Figs. 10a,b we present cross-sectional grayscale plots of Ertel potential vorticity at day 6.5 (the perspective is such that one is looking northwest and downward). The darker strato-

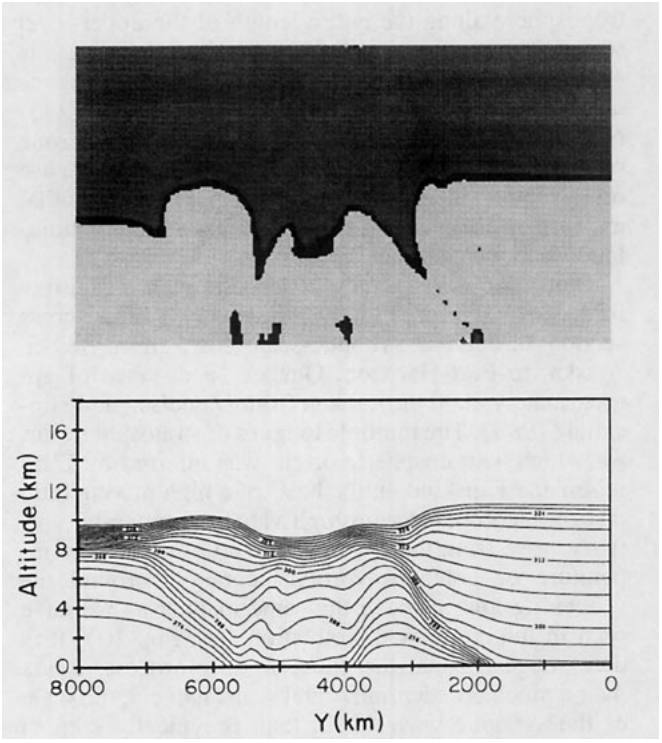

FIG. 11. (a) A meridional PV cross section (looking zonally) through the fold at the time of maximum descent (day 8 of model time) at x = 3261 km, and (b) the corresponding potential temperature field, with only values ≤ 330 K plotted using a contour interval of 5 K.

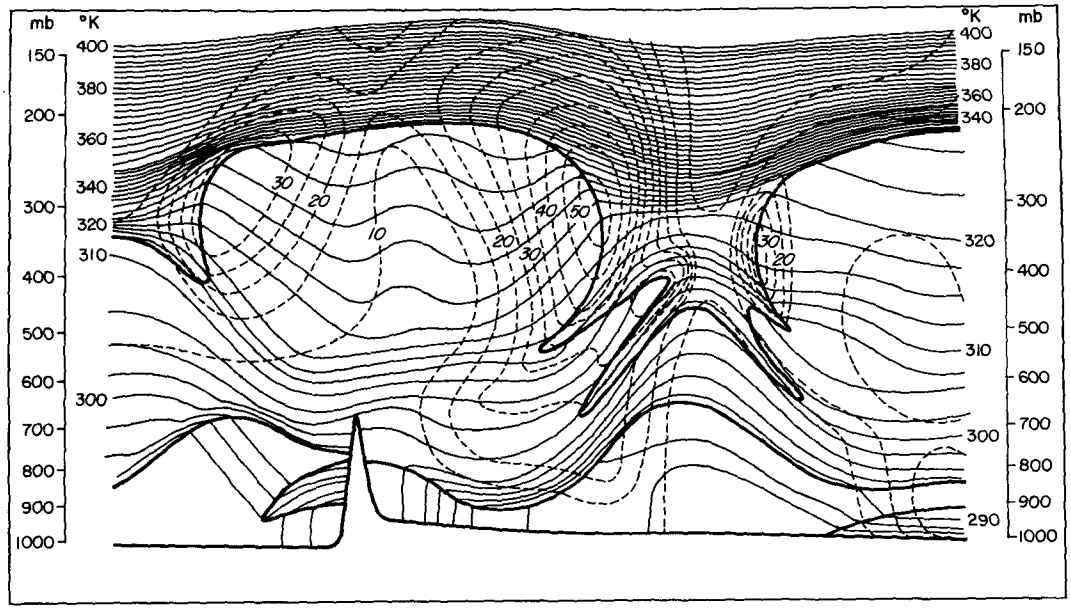

FIG. 12. Vertical cross section through a low from Bethel, Alaska, to Port Harrison, Quebec (a distance of approximately 8000 km), taken from Danielsen and Hipskind (1980). Solid contours are lines of constant potential temperature, with a contour interval of 2.5 K. The dashed lines are isotachs, with a contour interval of 5 m s^{-1}. The heavy contours denote the tropopause, the top of the boundary layer, and the earth's surface.

spheric values are seen to penetrate deeply into the troposphere along the entire length of the upper-level wave. The isentropic nature of the folding process is seen in a correspondence between these PV tongues and the fronts in the corresponding θ field (Fig. 11). Note in Fig. 11 the decreased slope of the frontal zone below 3 km and the greater height of the tropopause on the south side of the fold (cf. Fig. 1), features that are further enhanced in the higher baroclinicity simulation that we shall next discuss.

There is observational support for such a multiply folded structure. In Fig. 12 we display a broad cross section through a synoptic-scale low, from Bethel, Alaska, to Port Harrison, Quebec (a distance of approximately 8000 km), taken from Danielsen and Hipskind (1980). The multiple tongues of stratospheric air, for which a stratospheric origin was inferred by Danielsen and Hipskind on the basis of a high mixing ratio of ozone correlated with high values of potential vorticity, arise from the "wrapping" up of potential temperature or potential vorticity contours around the deepening low in much the same manner as we have seen in this numerical simulation (see Fig. 10). It is here suggested that the entire folding process occurs over a much broader horizontal scale, namely, the scale of the synoptic wave itself, than is typically seen in observational cross sections of folds such as that provided in Fig. 1; even though the fold may be only a few hundred kilometers wide in the cross-frontal direction, it will have an alongfront length equal to that of the front itself, with a greater vertical extent in those regions of particularly sharp horizontal temperature gradient.

2) THE SECOND SIMULATION: INTERMEDIATE BAROCLINICITY

This simulation was initialized using the mean state of Fig. 2b and the perturbation to this state whose structure was shown in Fig. 4b. The decreased time scale for the growth of the normal mode, compared to that in the case of climatological baroclinicity, is evident in the EKE time series (see Fig. 13a). Saturation of the wave occurs at day 6 and an unexpected alteration of its life cycle can be seen in the energetics and in the conversion terms (Fig. 13), beginning at day 4.5. This alteration takes the form of an extension of the eddy kinetic energy increase beyond the point of occlusion (which occurs at day 4.5) and a very slow decay of the conversion terms thereafter. The beginning of this life cycle modification, as we shall demonstrate, coincides with the introduction of stratospheric PV into the frontal regions of the surface low through a deep tropopause fold. Note the high values of the vertical Reynolds stress for this baroclinic wave compared to the levels realized in the simulation initialized with climatological baroclinicity, values indicative of a higher degree of barotropy.

The second EKE peak at day 9.5 is associated with an incipient frontal instability similar to that described for the first simulation, although the physical mechanism responsible for this secondary development seems

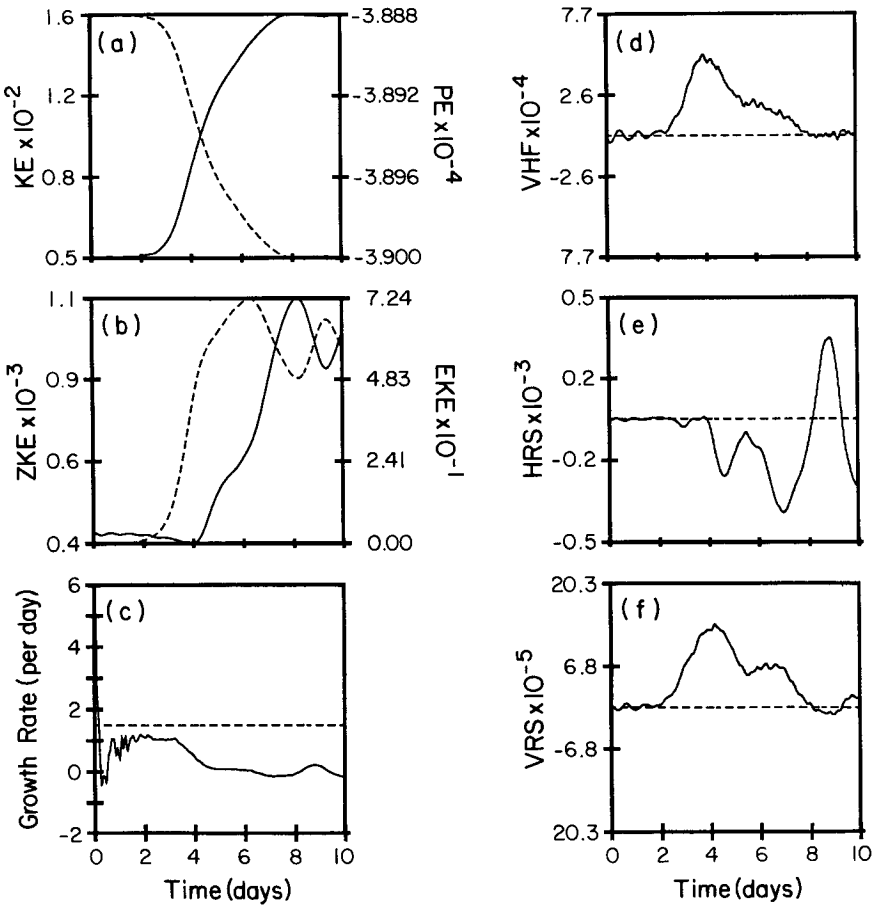

FIG. 13. As in Fig. 7 but now for the simulation initialized with intermediate baroclinicity.

to be more barotropic than baroclinic, a conjecture supported by the large HRS peak at day 9. The increased baroclinicity of the mean state has led to a decrease in the meridional scale, and the surface low is now so close to the parent front that there is a strong meridionally confined region of intense anticyclonic shear between the low and the westerly flow south of the front. This strong anticyclonic shear may be stabilizing the frontal region to the westward propagating disturbance seen in the previous simulation.

The growth rate of the wave in its linear phase (up to approximately day 3.5) is overpredicted by linear theory by approximately 40 percent. It is probable that, with the increasing baroclinicity of the mean state and the increased growth rates of the normal modes, the inertial oscillation from the initial field imbalance has not had sufficient time to decay before the fastest growing normal mode has risen to finite amplitude, thereby opening the door to wave–wave interactions in the early stages of the simulation. The evolution of the surface potential temperature field (Fig. 14) reveals the life cycle of the baroclinic wave rather clearly.

In Fig. 15 we present an isosurface plot of the tropopause (again represented by the 1 PVU surface). The basic vortical structure of the fold has not changed, but the extent of the vertical penetration into the troposphere is considerably enhanced, a consequence of the more intense horizontal deformation field associated with this more vigorous baroclinic wave. The maximum negative vertical velocity attained in this simulation is 15 cm s^{-1}, and the depth to which the fold descends is to within approximately 2 km of the lower boundary, well within the surface frontal region, at roughly day 4.75 of model time. The isentropic nature of the folding process is again clearly evident in a correspondence between the fold and the fronts in the potential temperature field (Fig. 16). Note in Fig. 16b the slope of the frontal zone within 2 km of the surface as compared to its slope above 2 km (cf. Fig. 1). The breakup of the fold occurs very soon after its descent into the surface vortex. The foot of the fold in this region becomes so narrow that the spatial filters in the model act to detach its deepest extremities, and we then see stratospheric PV being mixed into the troposphere

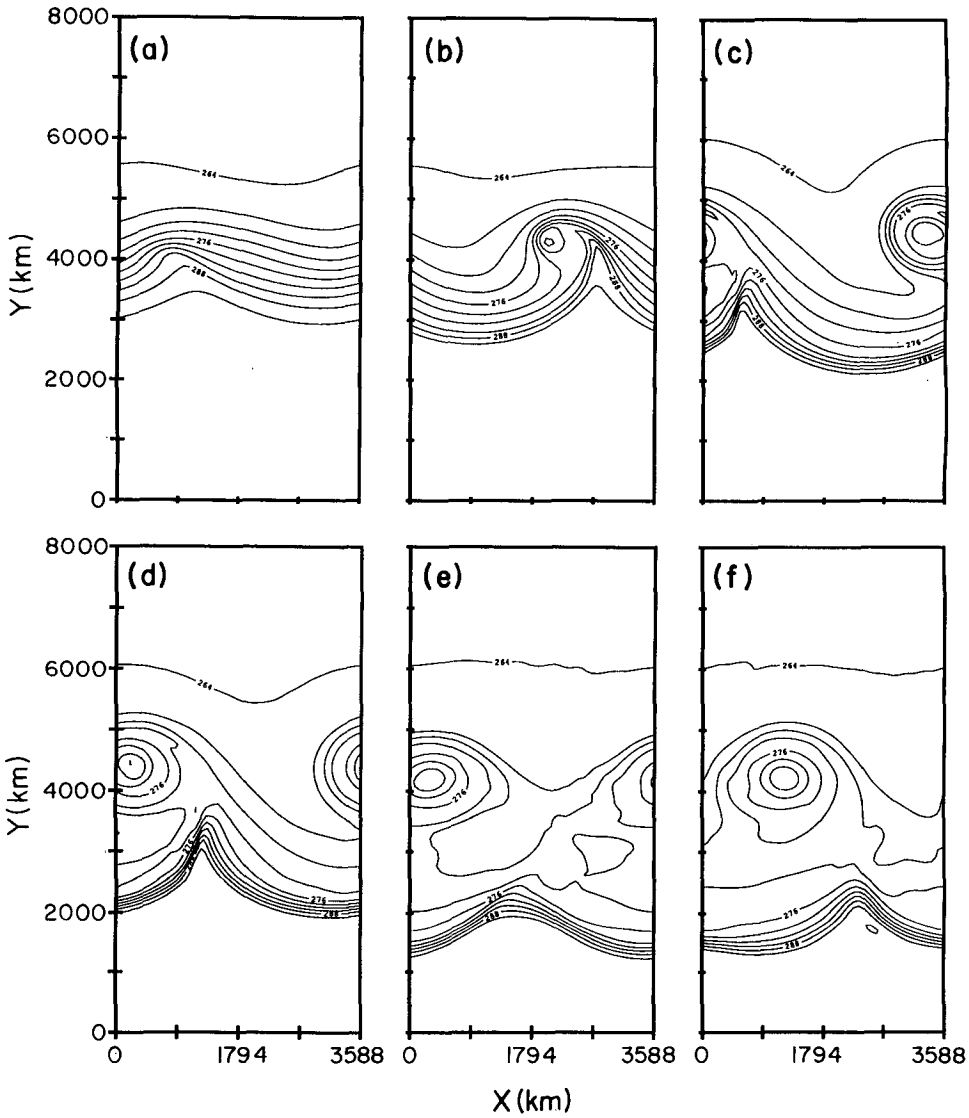

FIG. 14. Evolution of the surface potential temperature for the simulation initialized with intermediate baroclinicity. The domain is now 8000 × 3590 km. (a) Day 2.5, (b) day 3.5, (c) day 4.5, (d) day 5, (e) day 8.5, and (f) day 9.5. Note the decreased meridional scale and the decreased westward displacement of the low following the occlusion process. The maximum temperature in the core of the low is now 282 K with a contour interval of 3 K. A redevelopment of the cusp in the frontal zone is evident in (f).

irreversibly (although the islands of stratospheric PV that are detached are of approximately the grid scale and are soon eliminated by the filter). The time at which this breakup occurs corresponds to the alteration in the life cycle of the wave alluded to previously, suggesting that the barotropic decay of the wave is delayed by the introduction of stratospheric PV into the surface cyclone through this deep tropopause fold. The upper, broader part of the fold remains intruded into the troposphere, and the circulating vortex resulting from the upper-level wave remains as a positive PV anomaly throughout the remainder of the simulation.

3) THE THIRD SIMULATION: HIGH BAROCLINICITY

Although the fastest growing mode for this mean state was dominantly barotropic and was used to initialize the simulation, the wave that is actually delivered by the nonlinear integration is once more baroclinic. In fact, the energetics and the conversion terms for this simulation (Fig. 17) are very similar to those obtained for the model with intermediate baroclinicity, with the slight modification of increased VRS and decreased VHF as one would expect in this more strongly barotropic case. Furthermore, the growth rate of this

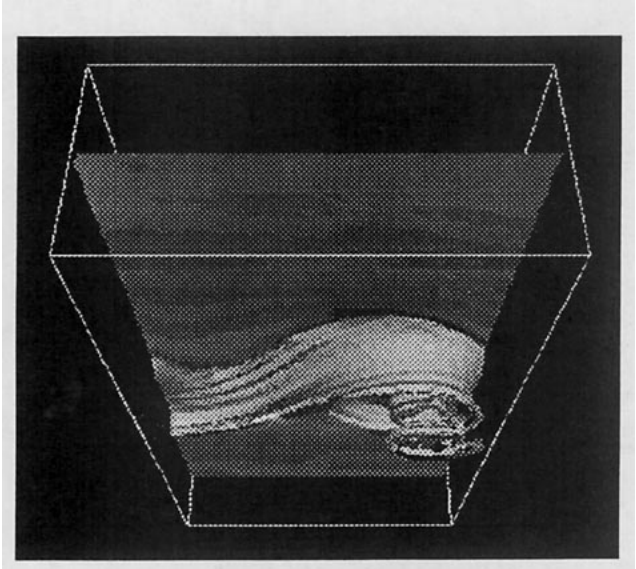

FIG. 15. Isosurface plot of the tropopause (the 1 PVU surface). Perspective is the same as in Fig. 9 only the zonal dimension is now 3590 km.

mode in its linear regime (up to approximately day 3) is roughly the same as that for the second simulation. Returning to the previously discussed Fig. 3c, one will observe that if this is indeed the baroclinic mode found in the linear theory (which does have a peak at roughly the same zonal wavelength) then once again linear theory overpredicts the growth rate, in this instance by approximately 50 percent.

The evolution of the surface potential temperature field (Fig. 18) proceeds much as in the previous simulation, with the exception that the temperature of the warm air in the core of the surface low is not as high as was found previously (278 K, as opposed to 282 K for the intermediate baroclinicity case, and 285 K for the climatological baroclinicity case). One additional difference in the results obtained in this strongly baroclinic example concerns the positioning of the low with respect to its associated cusp following occlusion. Comparing the three simulations, as the mean state baroclinicity is enhanced, the low detaches from this cusp with decreasing westward displacement, and for this third simulation the low is positioned practically due north of the cusp (see Figs. 8d, 14f, and 18f). This is a result of the increased zonal velocities as the baroclinicity is enhanced. The second peak in EKE corresponds to additional warm air being swept up from the cusp into the low, as occurred during the frontal instability seen previously, although a frontal disturbance is not clearly evident here.

The deformation of the tropopause also proceeds much as in the previous simulation (Fig. 19), although the maximum downward velocity obtained is 30 cm s^{-1}, indicating the action of a much more intense deformation field. The maximum depth to which the fold descends is again to a height of approximately 2 km above the surface at day 4 of model time (Fig. 20), and the tip of the fold is once more broken up by the spatial filters as it intrudes the low-level vortex. It seems rather clear that if we were able to compute the evolution of these disturbances with all sources of dissipation suppressed, then the tropopause folds generated by the most strongly baroclinic flows would actually descend to the ground.

4. Discussion and conclusions

Since observations of midlatitude zonal jets have invariably been averaged spatially and/or temporally, there is an arbitrariness in attempting to define a "realistic," eddy-free atmospheric mean state that is most appropriate as an initial state in life cycle analyses. It is worthwhile, therefore, to explore a range of possible initial states from which atmospheric eddies might evolve. The work presented in the previous sections describes an initial exploration of the effect of mean state baroclinicity not only on the process of deep synoptic-scale baroclinic instability but also on the tropopause folds that seem to be a generic feature of these instabilities.

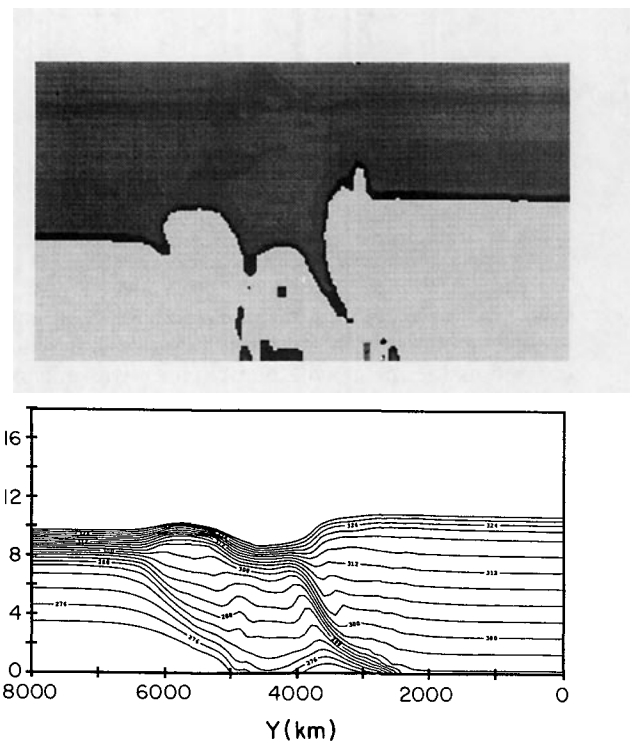

FIG. 16. (a) North–south cross-sectional view of PV (taken at x = 587 km looking in the zonal direction at day 4.75 of model time, the time of deepest descent). Note the classic meridional tilt of the fold, the increased depth of tropospheric penetration, and the boundary-generated PV. Note also the smaller horizontal scale of the fold as compared to that in Fig. 11. (b) The corresponding potential temperature field, with contours as in Fig. 11b.

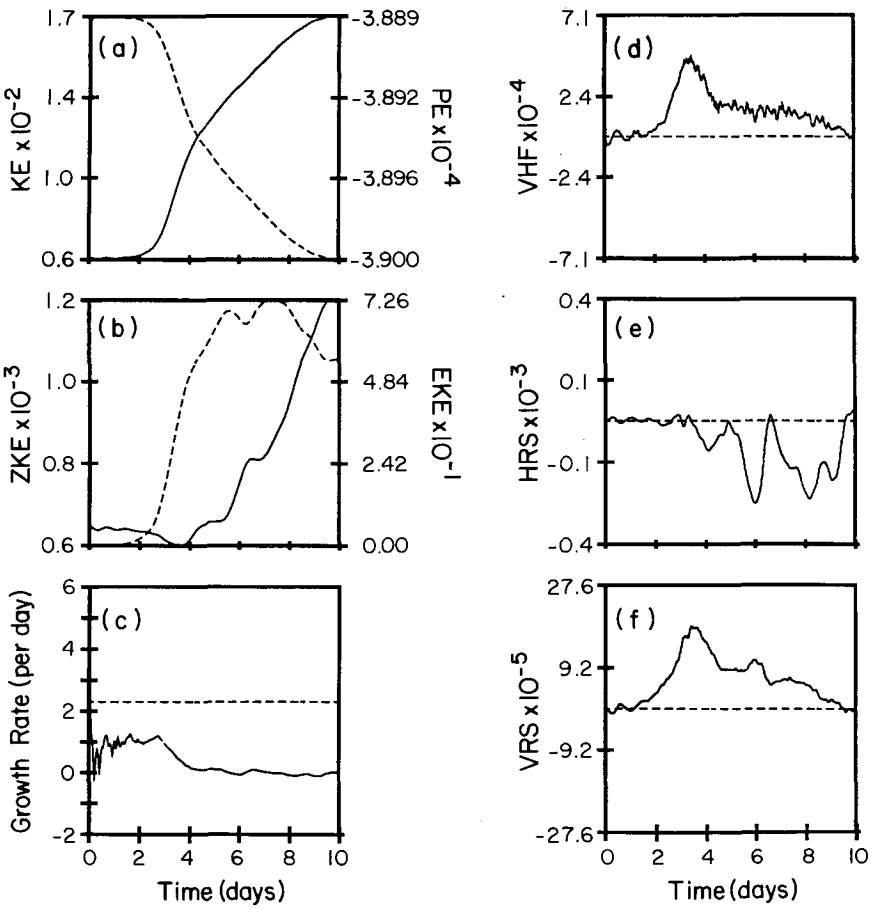

FIG. 17. As in Fig. 7 but now for the simulation initialized with maximum baroclinicity.

In all three cases analyzed, integration of the flow into the nonlinear regime delivered deep, synoptic-scale baroclinic waves whose meridional extent decreased as the mean state baroclinicity was enhanced. The vertical depth of tropospheric penetration and the horizontal extent of the tropopause folds accompanying these waves respectively increased and decreased with enhanced mean state baroclinicity.

A more rapid collapse of spatial gradients toward the grid scale is an inevitable consequence of the faster growing, more highly baroclinic waves. The ∇^6 spatial filter, although it is acting on the fields at all times, clearly has a more dramatic effect when and where the spatial scale of the disturbance becomes comparable to the grid size (e.g., in the surface frontal zones), and $2\Delta x$ noise becomes evident at this time. In fact, the surface fronts generated in the latter two simulations are of such narrow horizontal extent that they are spanned by at most six grid points and, were it not for the action of the filter, would in fact collapse to the grid scale. Of course, if infinite computational resources were available, one could simply increase the global resolution and thereby delay the impact of the artificial dissipation. One could closely examine the frontal dynamics and determine whether or not there is a minimum scale to which these fronts collapse before a dynamic arrest occurs [e.g., through the generation of internal waves (Ley and Peltier 1978)], a question whose answer would certainly allow us to more reasonably control the boundary PV generation. One simulation was performed (not shown) that was identical to the case of climatological baroclinicity, with the exception that the vertical resolution was doubled. It was found that the increased resolution did, in fact, delay the onset of PV nonconversion by roughly 2 days, although the inevitable onset of this effect nevertheless led to a PV deviation that eventually achieved the same magnitude.

Since the folds in our "almost" adiabatic simulations are located within the three-dimensional frontal zone, an increase in the mean state baroclinicity, with a corresponding increase in the deformation field associated with the growing baroclinic wave, drives the downward penetration of the fold more rapidly but also narrows its horizontal extent. For this reason, the diffusion operator has a more significant effect on a region of much greater vertical extent, and one expects the

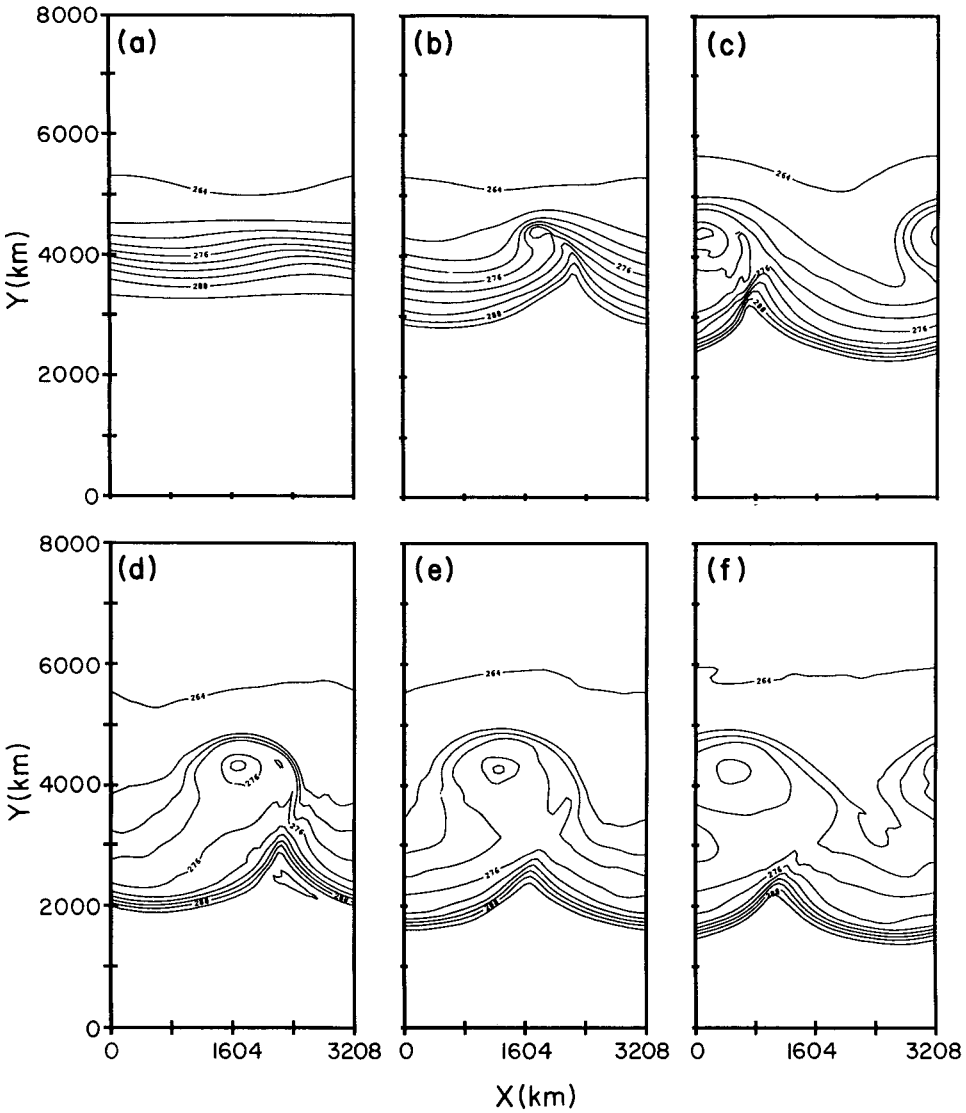

FIG. 18. Evolution of the surface potential temperature field for the simulation initialized with maximum baroclinicity. The domain is 8000 × 3208 km. (a) Day 1.5, (b) day 3, (c) day 4, (d) day 5, (e) day 7, and (f) day 9. Note the further decrease in meridional scale and the lower temperatures in the occluded low (maximum core temperature is 278 K).

conservation of potential vorticity to deteriorate as the initial baroclinicity is enhanced. In Fig. 21 we show the domain-averaged PV deviation for the three simulations. In all cases, the integrated value decreases after the onset of the occlusion process (which is representative of the collapse of the frontal zone to small scales), showing that the destruction of large stratospheric values of PV, as the fold becomes too narrow to be adequately resolved, is dominating the PV generation at the lower rigid boundary. In the analyses of Nakamura and Held (1989), for which there is a rigid upper lid at the tropopause as well as a rigid lower surface, there is a net generation of PV since there are positive contributions from both boundaries [as in the 3D simulations of Polavarapu and Peltier (1990)].

In our more realistic case, the rigid upper boundary is relatively insulated from large-scale motion because the baroclinic mode decays in the vertical above the tropopause, and the only positive contribution to PV generation is from the lower boundary. The PV values generated at the boundary, however, are relatively small (3 PVU maximum, but generally <1 PVU) compared to the larger stratospheric values that are being destroyed in the frontal zones; hence, we have a net decrease in PV. The PV destruction levels off after the fronts have been dissipated (visible in the first simu-

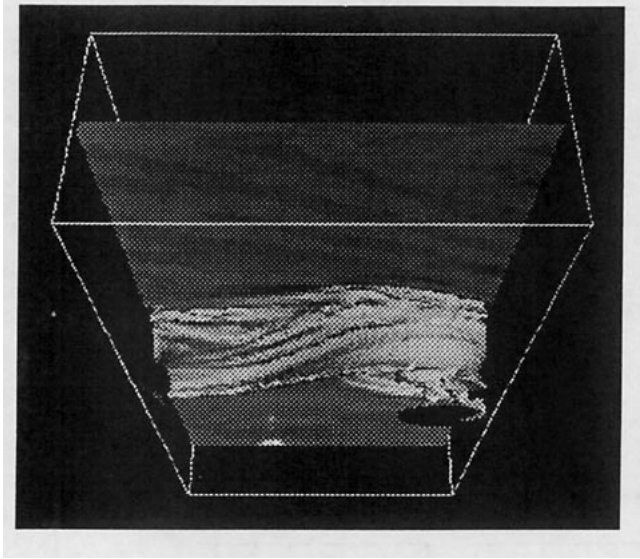

FIG. 19. As in Fig. 15 only taken at day 4 of model time.

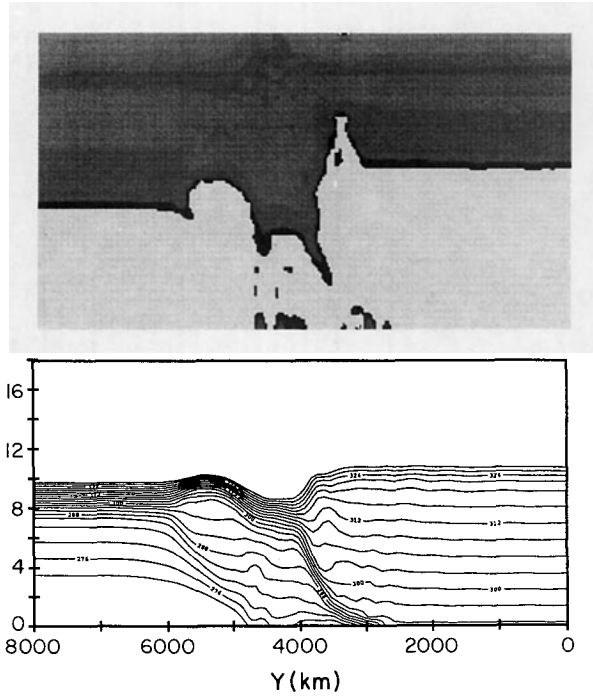

FIG. 20. As in Fig. 16 only taken at day 4 of mode time and at x = 717 km.

lation near day 11). This collapse of PV structures to the grid scale has been seen previously (e.g., Juckes and McIntyre 1987) in large-scale simulations.

This raises the fundamental issue of the utility of PV as a reliable tracer in models using some form of artificial dissipation. The isentropes that form frontal zones in a deep baroclinic wave, thereby delimiting a tropopause fold, intersect the surface, and the possibility arises for the boundary-generated PV to diffuse upward toward the fold; however, in our simulations the boundary-generated PV does not diffuse significantly up the frontal isentropes (although it was seen to reach an altitude of approximately 2 km in the third run) so that it is not difficult to distinguish in video animations the PV that is of stratospheric origin in the fold from the PV that has its origin at the lower rigid surface.

Holton (1990) and Haynes et al. (1991) have described a mechanism by which stratospheric air in the first few scale heights above the tropopause descends across isentropes in response to an eddy-induced mean zonal force, thereby making available for folding into the troposphere tracers characteristic of the middle stratosphere that would otherwise be inaccessible in an adiabatic process.

In a tropopause fold, either observational or numerical, the isentropes delimiting the fold are invariably members of, to use the terminology of Hoskins (1991), the "Underworld" and the "Middleworld." That is, the sloping frontal zone along which the fold descends and mixes is characterized by isentropes that either intersect the earth's surface or cross the tropopause but do not strike the earth's surface. One would, in this context, expect evidence of the "downward control" mechanism to manifest itself in the observational literature as excessively large readings of, for example, the ozone mixing ratio, readings more characteristic of Hoskins's "Overworld," during a tropopause fold event. To date (e.g., Danielsen 1980), the observed mixing ratios for ozone in the vicinity of a fold are of typical "Middleworld" values.

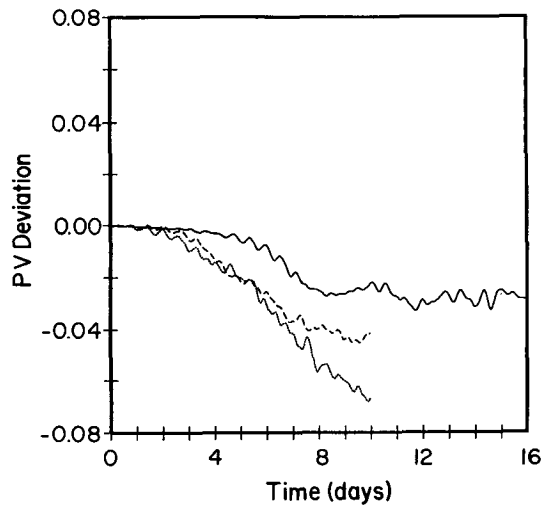

FIG. 21. The domain-averaged potential vorticity deviation for the three simulations. 1) Climatological baroclinicity (solid), 2) intermediate baroclinicity (dashed), and 3) maximum baroclinicity (dotted). Note the increasing rapidity of the onset of overall PV destruction as the background baroclinicity is turned up, and the leveling off of the PV destruction in 1) as the frontal zones are dissipated.

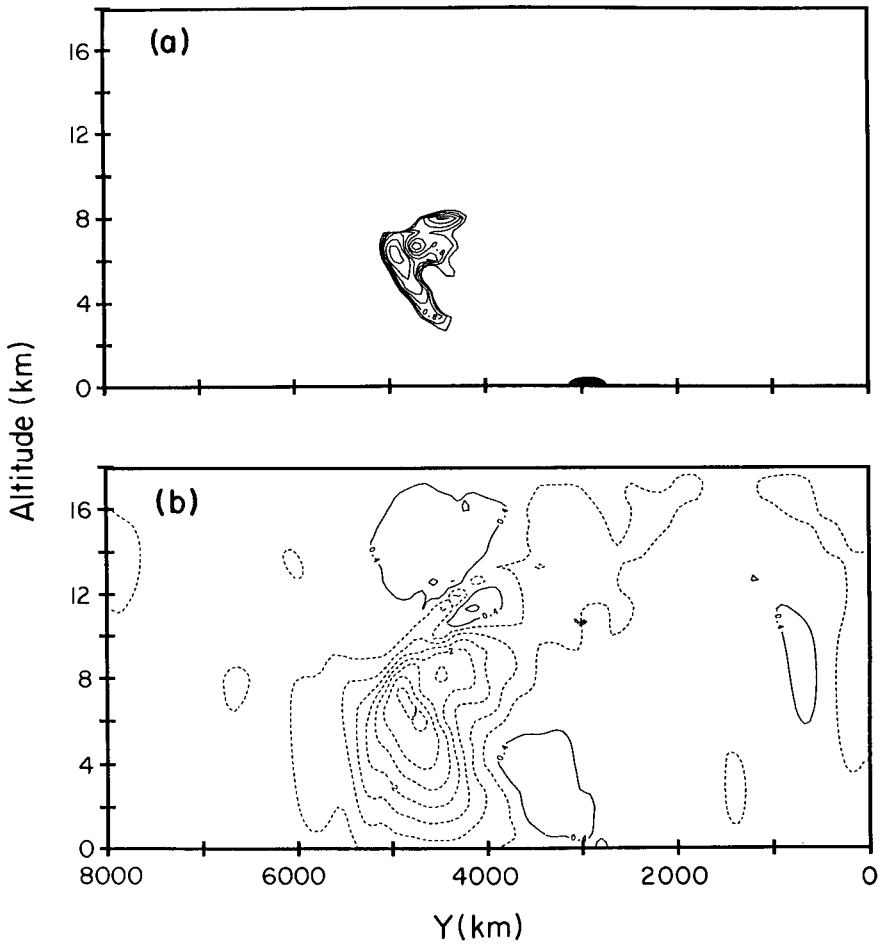

FIG. 22. Meridional cross sections of the Richardson number and vertical velocity for the simulation initialized with intermediate baroclinicity at day 3.5. Plotting conventions are such that (a) only values of the Richardson number ≤ 1 shown, with a contour interval of 0.1, and (b) the maximum negative vertical velocity is 4.1 cm s^{-1} with a contour interval of 0.7 cm s^{-1}. Note the low values of the Richardson number both in the descending air and in the surface frontal zone.

In the real atmosphere, there is clearly a variety of mechanisms at work in collapsing frontal zones that prevent the formation of infinite gradients. The issue, in the absence of the grid resolution that one might desire, of how these mechanisms might be rationally parameterized becomes important when features of interest are of the cross-frontal scale and, in the case of tropopause folds, this physics will play a vital role in the question of irreversible stratosphere/troposphere exchange. In our numerical simulations, the ∇^6 spatial filter is in large part responsible for the nonconservation of PV and for stratospheric values of PV being irreversibly mixed into the troposphere. The folds delivered by the latter two simulations were of such vertical extent that they descended deeply into the tight frontal regions of the surface cyclone, and islands of stratospheric PV values are seen to have "broken off" from the lower extremity of the fold and mixed into the surface cyclone. Whether this exchange is physically realistic or not is dependent on whether or not the artificial dissipation employed is accurately mimicking real mixing processes that do occur in this region of the flow.

Shapiro (1980) has, based on his observational work, estimated that turbulent mixing has a first-order impact on stratosphere/troposphere chemical exchange during a tropopause fold. It is known (e.g., Hoskins and Bretherton 1972) that the "foot" of the fold is a favored location for very low Richardson numbers, and hence that it is a prime site for the onset of turbulent mixing. The parameterization of subgrid-scale mixing (using first-order closure) that is supported in the present model was not used in the simulations reported here, but regions of Richardson number less than 0.25 are present in the surface frontal regions at the time of occlusion, and at the "foot" of the fold in the region

of strongest downward velocity, well before occlusion (Fig. 22).

The tropopause folds revealed in the simulations presented herein demonstrate that such folds are a generic feature of deep synoptic-scale baroclinic instability, with the "degree," or depth, of folding increasing with the increasing baroclinicity of the initial state. In making this assertion, we are of course assuming that the stratospheric buoyancy frequency is low enough that the tropopause may be substantially deformed since, if one increases the N_s/N_t ratio, one approaches the rigid-lid approximation and no folding is possible. In our analyses we have fixed the N_s/N_t ratio to a value appropriate for climatology and found that the folds generated in our numerical model very well match the general characteristics of those observed in nature (e.g., Fig. 1).

Surface frontogenesis and occlusion occur much as in previous tropospheric simulations of baroclinic wave life cycles, with the exception that the simulations initialized with highly baroclinic mean states had tropopause folds of such vertical extent that stratospheric values of potential vorticity were mixed into the surface cyclones at the time of occlusion, altering the physics of baroclinic wave decay in the classical life cycle (Nakamura and Held 1989).

In order to rigorously compare the simulated baroclinic life cycles to those observed in the atmosphere, similar high-resolution simulations should be performed on the sphere. From analyses of baroclinic waves on the β plane, however, the basic life cycle (i.e., the growth and occlusion of the wave) remains the same as on the f plane, with distortions of shape as the low moves northward throughout the process. However, the vertical shape of the tropopause folds will not be affected by the earth's curvature because the frontal zones in which the fold descends is so strongly confined in the horizontal. The slope of the frontal zone, however, may change as a result of differential influences of β on the surface and upper lows, thereby changing the slope of the fold.

A more interesting effect, and more pertinent to the current issue on the use of PV as a tracer of stratospheric air, would be to include diabatic effects in the model. Our model, being originally a cloud model, allows for the incorporation of moisture and, for synoptic-scale baroclinic waves, the diabatic effects of latent heat release near the frontal zones could have a significant effect on stratosphere/troposphere exchange when, as in our latter simulations, the fold penetrates the surface frontal zones. Use of the eddy mixing parameterization (and the incorporation of moisture effects) in the model would perhaps give a physically more realistic picture of the mixing processes that doubtless occur within a tropopause fold, since the Richardson number does drop below 0.25 both at the foot of the fold as it is descending and also in the surface frontal zones. The physical relevance of the irreversible transfer of stratospheric values of PV to the troposphere seen in the simulations performed here, however, is limited by the extent to which the artificial dissipation that we employ successfully mimics nature.

APPENDIX

Definition of E Matrix

Equations (2.17)–(2.19) define the matrix eigenvalue problem

$$\sigma \mathbf{V}_i = E_{ij}\mathbf{V}_j \tag{4.1}$$

for the vector $\mathbf{V} = (U_{\kappa\nu}, V_{\kappa\nu}, \Theta_{\kappa\nu})$. The matrix elements E_{ij} for the f-plane anelastic system using a pseudospectral weighting of Θ (for which the basis function $H_{\lambda\nu} = \exp^{i\pi\lambda x/2L}\delta(z - z_\nu)$ are used in the thermodynamic equation) are given below. The coordinate system is the usual (x, y, z) = (zonal, meridional, vertical) and has been nondimensionalized according to the following scheme:

$$x = \frac{NH}{\alpha}x^* \quad y = \frac{NH}{f_0}y^* \quad z = Hz^* \quad t = \frac{1}{\alpha}t^*$$

$$u = NHu^* \quad v = \frac{\alpha NH}{f_0}v^* \quad w = \alpha Hw^*$$

$$\theta = \frac{\theta_0}{g}N^2H\theta^* \quad \phi = N^2H^2\phi^*,$$

where the values of the units have been chosen as

$$N = 10^{-2}\ \mathrm{s}^{-1} \quad H = 24\ \mathrm{km} \quad \alpha = 10^{-5}\ \mathrm{s}^{-1}$$

$$\theta_0 = 273\ \mathrm{K} \quad f_0 = 10^{-4}\ \mathrm{s}^{-1} \quad g = 9.8\ \mathrm{m\ s}^{-2}.$$

The reader is referred to Polavarapu (1989) for a full derivation that includes the β effect, which has not been employed in the analyses that we have performed:

$$E_{11} = -I^1_{\kappa\mu\lambda\nu} + \left[i\left(\frac{\lambda\pi}{2L}\right)\Big/(\nu\pi)\right] I^2_{\kappa\mu\lambda\nu} - i\left(\frac{\kappa\pi}{2L}\right)\left(\frac{f_0}{\alpha}\right)^2\left[J^1_{\kappa\mu\lambda\nu} - i\left(\frac{\lambda\pi}{2L}\right)\Big/(\nu\pi)J^3_{\kappa\mu\lambda\nu}\right] \tag{4.2}$$

$$E_{12} = \left(\frac{f_0}{\alpha}\right)^2\delta_{\mu\nu}\delta_{\kappa\lambda} + ib/(\nu\pi)I^2_{\kappa\mu\lambda\nu} - i\left(\frac{\kappa\pi}{2L}\right)\left(\frac{f_0}{\alpha}\right)^2[J^2_{\kappa\mu\lambda\nu} - ib/(\nu\pi)J^3_{\kappa\mu\lambda\nu}] \tag{4.3}$$

$$E_{13} = -\left(\frac{f_0}{\alpha}\right)^2 i\left(\frac{\kappa\pi}{2L}\right)J^4_{\kappa\mu\lambda\nu} \tag{4.4}$$

$$E_{21} = -I^3_{\kappa\mu\lambda\nu} + i\left(\frac{\lambda\pi}{2L}\right)\Big/(\nu\pi)I^5_{\kappa\mu\lambda\nu} - ib\left[J^1_{\kappa\mu\lambda\nu} - i\left(\frac{\lambda\pi}{2L}\right)\Big/(\nu\pi)J^3_{\kappa\mu\lambda\nu}\right] \quad (4.5)$$

$$E_{22} = -I^4_{\kappa\mu\lambda\nu} + \frac{ib}{(\nu\pi)}I^5_{\kappa\mu\lambda\nu} - ib\left[J^2_{\kappa\mu\lambda\nu} - \frac{ib}{(\nu\pi)}J^3_{\kappa\mu\lambda\nu}\right] \quad (4.6)$$

$$E_{23} = -ibJ^4_{\kappa\mu\lambda\nu} \quad (4.7)$$

$$E_{31} = -I^6_{\kappa\mu\lambda\nu} + i\left(\frac{\lambda\pi}{2L}\right)\Big/(\nu\pi)I^7_{\kappa\mu\lambda\nu} \quad (4.8)$$

$$E_{32} = \frac{ib}{(\nu\pi)}I^7_{\kappa\mu\lambda\nu} \quad (4.9)$$

$$E_{33} = -I^8_{\kappa\mu\lambda\nu}, \quad (4.10)$$

where the quantities $I^i_{\kappa\mu\lambda\nu}$ and $J^i_{\kappa\mu\lambda\nu}$ are defined in terms of the Galerkin basis functions and the integral operator (2.16) by the following expressions:

$$I^1_{\kappa\mu\lambda\nu} = \left[-i\left(\frac{k\pi}{2L}\right)\langle F^*_{\kappa\mu}\bar{v}F_{\lambda\nu}\rangle + ib\langle F^*_{\kappa\mu}\bar{u}F_{\lambda\nu}\rangle - (\nu\pi)\langle F^*_{\kappa\mu}\bar{w}G_{\lambda\nu}\rangle + \langle F^*_{\kappa\mu}\partial_y\bar{v}F_{\lambda\nu}\rangle\right]\Big/(1+\delta_{\mu 0}) \quad (4.11)$$

$$I^2_{\kappa\mu\lambda\nu} = -\frac{(\nu\pi)}{j\pi}D^{-1}_{j\nu}\langle F^*_{\kappa\mu}\partial_z\bar{v}G_{\lambda\nu}\rangle/(1+\delta_{\mu 0}) \quad (4.12)$$

$$I^3_{\kappa\mu\lambda\nu} = [-\langle F^*_{\kappa\mu}\partial_y\bar{u}F_{\lambda\nu}\rangle/(1+\delta_{\mu 0}) + \delta_{\kappa\lambda}\delta_{\mu\nu} \quad (4.13)$$

$$I^4_{\kappa\mu\lambda\nu} = \left[-i\left(\frac{\lambda\pi}{2L}\right)\langle F^*_{\kappa\mu}\bar{v}F_{\lambda\nu}\rangle + ib\langle F^*_{\kappa\mu}\bar{u}F_{\lambda\nu}\rangle - (\nu\pi)\langle F^*_{\kappa\mu}\bar{w}G_{\lambda\nu}\rangle\right]\Big/(1+\delta_{\mu 0}) \quad (4.14)\text{–}(4.15)$$

$$I^5_{\kappa\mu\lambda\nu} = \langle F^*_{\kappa\mu}\partial_z\bar{u}G_{\lambda\nu}\rangle/(1+\delta_{\mu 0}) \quad (4.16)$$

$$I^6_{\kappa\mu\lambda\nu} = -D^{-1}_{\mu\gamma}\langle H^*_{\kappa\mu}\partial_y\bar{\theta}F_{\lambda\nu}\rangle \quad (4.17)$$

$$I^7_{\kappa\mu\lambda\nu} = D^{-1}_{\mu\gamma}\langle H^*_{\kappa\mu}\partial_z\bar{\theta}G_{\lambda\nu}\rangle \quad (4.18)$$

$$I^8_{\kappa\mu\lambda\nu} = D^{-1}_{\mu\gamma}\left[-i\left(\frac{\kappa\pi}{2L}\right)\langle H^*_{\kappa\mu}\bar{v}F_{\lambda\nu}\rangle + ib\langle H^*_{\kappa\mu}\bar{u}F_{\lambda\nu}\rangle - (\nu\pi)\langle H^*_{\kappa\mu}\bar{w}G_{\lambda\nu}\rangle\right] \quad (4.19)\text{–}(4.20)$$

$$J^1_{\kappa 0\lambda\nu} = \left[ib\delta_{\nu 0}\delta_{\kappa\lambda} + i\left(\frac{\lambda\pi}{2L}\right)\langle F^*_{\kappa 0}\partial_y\bar{v}F_{\lambda\nu}\rangle - ib\langle F^*_{\kappa 0}\partial_y\bar{u}F_{\lambda\nu}\rangle + (\nu\pi)\langle F^*_{\kappa 0}\partial_y\bar{w}G_{\lambda\nu}\rangle\right]\Big/L_{\kappa 0} \quad (4.21)$$

$$J^2_{\kappa 0\lambda\nu} = -\left(\frac{f_0}{\alpha}\right)^2\delta_{\nu 0}\left[i\left(\frac{\lambda\pi}{2L}\right)\delta_{\kappa\lambda}\right]\Big/L_{\kappa 0} \quad (4.22)$$

$$J^3_{\kappa 0\lambda\nu} = \left[-i\left(\frac{\lambda\pi}{2L}\right)\langle F^*_{\kappa 0}\partial_z\bar{v}G_{\lambda\nu}\rangle + ib\langle F^*_{\kappa 0}\partial_z\bar{u}G_{\lambda\nu}\rangle + (\nu\pi)\langle F^*_{\kappa 0}\partial_z\bar{w}F_{\lambda\nu}\rangle - \langle F^*_{\kappa 0}\bar{w}d_zRG_{\lambda\nu}\rangle\right]\Big/L_{\kappa 0}, \quad (4.23)$$

where

$$R(z) = \frac{1}{\rho}\frac{d\rho}{dz}$$

$$J^4_{\kappa 0\lambda\nu} = 0 \quad (4.24)$$

$$J^1_{\kappa\mu\lambda\nu} = J^2_{\kappa\mu\lambda\nu} = J^3_{\kappa\mu\lambda\nu} = 0 \quad (4.25)$$

$$J^4_{\kappa\mu\lambda\nu} = \frac{-1}{\mu\pi}\langle G^*_{\kappa\mu}F_{\lambda\nu}\rangle \quad (4.26)$$

$$L_{\kappa 0} = \left(\frac{f_0}{\alpha}\right)^2\left(\left(\frac{\kappa\pi}{2L}\right)\right)^2 + b^2 \quad (4.27)$$

and

$$D_{\gamma\nu} = 2\int_0^1 \delta(z^* - z^*_\gamma)\cos((\nu\pi)z^*)dz^* \quad (4.28)$$

is the collocation matrix used in the thermodynamic equation.

REFERENCES

Andrews, D. G., J. R. Holton, and C. B. Leovy, 1987: *Middle Atmosphere Dynamics.* Int. Geophys. Ser., Vol. 40. Academic Press, 489 pp.

Charney, J. G., 1947: The dynamics of long waves in a baroclinic westerly current. *J. Meteor.*, **4,** 135–163.

Clark, T., 1977: A small-scale dynamic model using a terrain-following coordinate transformation. *J. Comput. Phys.*, **24,** 186–215.

Danielsen, E. F., 1968: Stratospheric–tropospheric exchange based on radioactivity, ozone and potential vorticity. *J. Atmos. Sci.*, **25,** 502–518.

——, 1980: Stratospheric source for unexpectedly large values of ozone measured over the Pacific Ocean during Gametag, August 1977. *J. Geophys. Res.*, **85,** 401–412.

——, and J. W. Diercks, 1967: A study of the tropopause based on numerical integration of the potential vorticity equation. Dept. of Meteorology, The Pennsylvania State University, Rep. NYO-3317-1, 43 pp.

——, and V. A. Mohnen, 1977: Project Dustorm report: Ozone transport, in situ measurements, and meteorological analyses of tropopause folding. *J. Geophys. Res.*, **82,** 5867–5877.

——, and R. S. Hipskind, 1980: Stratospheric–tropospheric exchange at polar latitudes in summer. *J. Geophys. Res.*, **85,** 393–400.

Dritschel, D. G., P. H. Haynes, M. N. Juckes, and T. G. Shepherd: The stability of a two-dimensional vorticity filament under uniform strain. *J. Fluid Mech.*, **230,** 647–665.

Eady, E. T., 1949: Long waves and cyclone waves. *Tellus,* **1,** 33–52.

Edmon, H. J., Jr., B. J. Hoskins, and M. E. McIntyre, 1980: Eliassen–Palm cross sections for the troposphere. *J. Atmos. Sci.,* **37,** 2600–2616.

Eliassen, A., and E. Palm, 1960: On the transfer of energy in stationary mountain waves. *Geophys. Norv.,* **22,** 1–23.

Ertel, H., 1942: Ein neuer hydrodynamischer Wirbelsatz. *Meteor. Z.,* **59,** 277–281.

Gall, R., 1976: A comparison of linear baroclinic instability of a general circulation model. *J. Atmos. Sci.,* **33,** 349–373.

Geisler, J. E., and R. R. Garcia, 1977: Baroclinic instability at long wavelengths on a β-plane. *J. Atmos. Sci.,* **34,** 311–321.

Gidel, L. T., and M. A. Shapiro, 1979: The role of clear air turbulence in the production of potential vorticity in the vicinity of upper tropospheric jet-stream frontal systems. *J. Atmos. Sci.,* **36,** 2125–2138.

Haynes, P. H., C. J. Marks, M. E. McIntyre, T. G. Shepherd, and K. P. Shine, 1991: On the "downward control" of extratropical diabatic circulations by eddy-induced mean zonal forces. *J. Atmos. Sci.,* **48,** 651–678.

Heckley, W. A., and B. J. Hoskins, 1982: Baroclinic waves and frontogenesis in a non-uniform potential vorticity semi-geostrophic model. *J. Atmos. Sci.,* **39,** 1999–2016.

Holton, J. R., 1979: *An Introduction to Dynamic Meteorology.* 2d ed. Int. Geophys. Ser., Vol. 23. Academic Press, 391 pp.

——, 1990: On the global exchange of mass between the stratosphere and troposphere. *J. Atmos. Sci.,* **47,** 392–395.

Hoskins, B. J., 1972: Non-Boussinesq effects and further development in a model of upper tropospheric frontogenesis. *Quart. J. Roy. Meteor. Soc.,* **98,** 532–541.

——, 1991: Towards a PV–Θ view of the general circulation. *Tellus,* **43AB,** 27–35.

——, and F. P. Bretherton, 1972: Atmospheric frontogenesis models: Mathematical formulation and solution. *J. Atmos. Sci.,* **29,** 11–37.

——, and N. V. West, 1979: Baroclinic waves and frontogenesis. Part II: Uniform potential vorticity jet flows—Cold and warm fronts. *J. Atmos. Sci.,* **36,** 1663–1679.

Juckes, M. N., and M. E. McIntyre, 1987: A high-resolution, one-layer model of breaking planetary waves in the stratosphere. *Nature,* **328,** 590–596.

Keyser, D., B. D. Schmidt, and D. G. Duffy, 1989: A technique for representing three-dimensional vertical circulations in baroclinic disturbances. *Mon. Wea. Rev.,* **117,** 2463–2493.

Leith, C. E., 1980: Nonlinear normal mode initialization and quasi-geostrophic theory. *J. Atmos. Sci.,* **37,** 958–968.

Ley, B. E., and W. R. Peltier, 1978: Wave generation and frontal collapse. *J. Atmos. Sci.,* **35,** 3–17.

Moore, G. W. K., 1987: Frontogenesis in a continuously varying potential vorticity fluid. *J. Atmos. Sci.,* **44,** 761–770.

——, and W. R. Peltier, 1987: Cyclogenesis in frontal zones. *J. Atmos. Sci.,* **44,** 384–409.

——, and ——, 1989: Frontal cyclogenesis and the geostrophic momentum approximation. *Geophys. Astrophys. Fluid Dyn.,* **45,** 183–197.

Newell, R. E., J. W. Kidson, D. G. Vincent, and G. J. Boer, 1972: *The General Circulation of the Tropical Atmosphere and Interactions with Extratropical Latitudes.* Vol. I. The MIT Press, 258 pp.

Polavarapu, S. M., 1989: Synoptic-scale baroclinic wave life-cycles. Ph.D. thesis, Dept. of Physics, University of Toronto.

——, and W. R. Peltier, 1990: The structure and nonlinear evolution of synoptic scale cyclones: Life cycle simulations with a cloud-scale model. *J. Atmos. Sci.,* **47,** 2645–2672.

——, and ——, 1992: On the formation of small-scale cyclones in numerical simulations of synoptic-scale baroclinic wave life cycles: Secondary instability at the cusp. *J. Atmos. Sci.,* **50,** 1047–1057.

——, and ——, 1993: The structure and nonlinear evolution of synoptic-scale cyclones: Wave–mean flow interaction and equilibration. *J. Atmos. Sci.,* **50,** 3164–3184.

Reed, R. J., 1955: A study of a characteristic type of upper-level frontogenesis. *J. Meteor.,* **12,** 226–237.

——, and F. Sanders, 1953: An investigation of the development of a mid-tropospheric frontal zone and its associated vorticity field. *J. Meteor.,* **10,** 338–349.

Shapiro, M. A., 1980: Turbulent mixing within tropopause folds as a mechanism for the exchange of chemical constituents between the stratosphere and troposphere. *J. Atmos. Sci.,* **37,** 994–1004.

Simmons, A. J., and B. J. Hoskins, 1976: Baroclinic instability on the sphere: Normal modes of the primitive and quasi-geostrophic equations. *J. Atmos. Sci.,* **33,** 1454–1477.

——, and ——, 1977: Baroclinic instability on the sphere: Solutions with a more realistic tropopause. *J. Atmos. Sci.,* **34,** 581–588.

Staley, D. O., 1960: Evaluation of potential vorticity changes near the tropopause and the related vertical motions, vertical advection of vorticity, and transfer of radioactive debris from stratosphere to troposphere. *J. Meteor.,* **17,** 591–620.

World Meteorological Organization (WMO), 1985: *Atmospheric Ozone.* Vol. 1. Global Ozone Research and Monitering Prôject Report No. 16, NASA, Washington, DC.